INSTITUT DE FRANCE
Académie des sciences

Comptes Rendus

Géoscience

Sciences de la Planète

Roberto Moretti

Redox behavior of degassing magmas: critical review and comparison of glass-based oxybarometers with application to Etna volcano

Volume 354, Special Issue S1 (2022), p. 249-280

Published online: 11 July 2022
Issue date: 1 December 2022

https://doi.org/10.5802/crgeos.135

Part of Special Issue: Glass, an ubiquitous material
Guest editor: Daniel Neuville (Université de Paris, Institut de physique du globe de Paris, CNRS)

Les Comptes Rendus. Géoscience — Sciences de la Planète *sont membres du Centre Mersenne pour l'édition scientifique ouverte*
www.centre-mersenne.org
e-ISSN : 1778-7025

Comptes Rendus
Géoscience — Sciences de la Planète
2022, Vol. 354, Special Issue S1, p. 249-280
https://doi.org/10.5802/crgeos.135

Glass, an ubiquitous material / *Le verre, un matériau omniprésent*

Redox behavior of degassing magmas: critical review and comparison of glass-based oxybarometers with application to Etna volcano

Comportement redox du dégazage magmatique : revue critique et comparaison des oxybaromètres basés sur les verres avec application au volcan Etna

Roberto Moretti *a, b*

[a] Université de Paris Cité, Institut de physique du globe de Paris, UMR 7154 CNRS, 1 rue Jussieu, 75238 Paris, France

[b] Observatoire volcanologique et sismologique de Guadeloupe, Institut de physique du globe de Paris, Le Houelmont, 97113 Gourbeyre, France

E-mail: moretti@ipgp.fr

Abstract. Glass/melt inclusions are repositories of polybaric magma physiochemical interactions. They are fundamental to retrieve the conditions of fluid saturation and magma oxidation state. The latter is usually reported as oxygen fugacity, which is a key thermodynamic variable: involved in such polybaric physiochemical interactions, fO_2 affects melt saturation properties and fixes the speciation of fluids discharged by magmatic systems either up to volcanic craters or feeding hydrothermal systems. Several oxybarometers have been proposed, based on iron and sulfur oxidation states. In this study I summarize their main features and show their performances for 1-bar and fluid-saturated andesitic and basaltic melts. I then show that any assessment of magma redox behavior that does not account for the melt reactivity, driven by melt polymerization and the so-called oxygen electrode in association with iron or sulfur redox couples, may fail in determining the actual contribution of the composition to the observed variations of iron and sulfur oxidation states, resulting in potentially biased fO_2 estimates. In the case of Etna volcano, by using a well-established ionic-polymeric approach we show that a major control is the dehydration taking place during magmatic differentiation and magma ascent. Dehydration determines a slight iron oxidation down to around 2.5 wt% in dissolved water, but further dehydration taking place up to the surface results in iron reduction. This dual behavior, related to a change of trivalent iron speciation, is reproduced by reactive ionic-polymeric approaches and for the Etna basalt it is predicted also for constant fO_2. Such a modulation of the redox state due to water dissolution cannot be reproduced by empirical formulations.

Résumé. Les inclusions vitreuses sont les dépositaires des interactions physico-chimiques polybares des magmas. Elles sont fondamentales pour déterminer les conditions de saturation des fluides et l'état d'oxydation du magma. Ce dernier est généralement donné sous forme de fugacité de l'oxygène, qui est une variable thermodynamique clé : impliquée dans ces interactions physico-chimiques

polybares, la fO_2 affecte les propriétés de saturation du magma et fixe la spéciation des fluides qui sont déchargés par les systèmes magmatiques jusqu'aux cratères volcaniques ou qui alimentent les systèmes hydrothermaux. Plusieurs oxybaromètres ont été proposés, basés sur l'état d'oxydation du fer et du soufre. Dans cette étude, je résume leurs principales caractéristiques et montre leurs performances pour des liquides andésitiques et basaltiques à 1 bar et saturés en fluides. Je montre ensuite que toute évaluation du comportement redox du magma qui ne tient pas compte de la réactivité du liquide silicaté, entraînée par sa polymérisation et la soi-disant électrode à oxygène en association avec les couples redox du fer ou du soufre, peut échouer dans la détermination de la contribution réelle de la composition aux variations observées de l'état d'oxydation du fer et du soufre, ce qui entraîne des estimations potentiellement biaisées de fO_2. Dans le cas du volcan Etna, en utilisant une approche ionique-polymérique bien établie, nous montrons qu'un contrôle majeur est donné par la déshydratation qui a lieu pendant la différenciation magmatique et l'ascension du magma. La déshydratation détermine une légère oxydation du fer jusqu'à environ 2.5% en poids dans l'eau dissoute, mais une déshydratation plus poussée ayant lieu jusqu'à la surface produit une réduction du fer. Ce double comportement, lié à un changement de spéciation du fer trivalent, est reproduit par des approches ioniques-polymériques réactives et, pour le basalte de l'Etna, il est également prédit pour une fO_2 constante. Une telle modulation de l'état redox due à la dissolution de l'eau ne peut être reproduite par des formulations empiriques.

Keywords. Melt/glass inclusions, Oxygen fugacity, Sulfur speciation, Iron amphoteric behavior, Polymerization, Etna, Melt dehydration.

Mots-clés. Inclusions vitreuses, Fugacité d'oxygène, Spéciation du soufre, Comportement amphotère du fer, Polymérisation, Etna, Déshydratation.

Published online: 11 July 2022, Issue date: 1 December 2022

1. Introduction and rationale

Magma is the most important transport agent throughout our planet. It is in fact the main carrier of oxygen through Earth's interiors up to the surface, and its liquid portion, the silicate melt, operates as a very efficient high-temperature chemical solvent for metal oxides as well as volatile components [e.g., Trémillon, 1974, Allanore, 2013, 2015, Cicconi et al., 2020a, Moretti and Neuville, 2021, Moretti and Ottonello, 2022, Papale et al., 2022]. The redox state of magmas then refers to the ensemble of conditions and variables governing the oxidation state of metals, volatiles and the species they form, either dissolved in the melt or exsolved in a coexisting fluid. Therefore, parameterization of the redox state is fundamental to assess mass and energy transfer in magmas and particularly its phase equilibria and the P–T conditions at which these take place. Although this is well known in petrology, because phase equilibria are deeply impacted by the relative proportions of FeO and Fe_2O_3, knowledge of redox states during magma differentiation and particularly during magma ascent is highly important to help reconstruct the architecture of volcanic plumbing systems and the dynamics of rising natural magmas and associated fluids. Both of these aspects require the evaluation of the speciation of volcanic fluids and their state of saturation with the melt, making the redox state of the magma a main parameter of this evaluation, even if not explicitly treated [e.g., Spilliaert et al., 2006, Aiuppa et al., 2007, 2009, 2010, 2016, 2017, 2018, 2022, Mangiacapra et al., 2008, Barsanti et al., 2009, Allard, 2010, Arienzo et al., 2010, 2016, Blundy et al., 2010, Allard et al., 2016, Edmonds et al., 2010, Edmonds and Wallace, 2017, Esposito et al., 2011, Oppenheimer et al., 2011, Mormone et al., 2011, Pino et al., 2011, Moretti et al., 2013a,b, 2018, 2019, Moussallam et al., 2014, 2016, 2019, Hartley et al., 2014, 2017, Le Losq et al., 2015, Wallace et al., 2015b, Brounce et al., 2017, Allison et al., 2021, Gennaro et al., 2020, Paonita et al., 2021]. In particular, tracking the evolution in time and depth of the volcanic fluid phase has become central for the geochemical monitoring of volcanic activity and for eruption forecasting. This demands the adoption of models for melt–fluid saturation accounting for the redox state, which is made by profiling the evolution of the amount of oxygen available to react with elements in the system, that is, the fugacity of molecular oxygen, fO_2 [Moretti and Papale, 2004, Burgisser and Scaillet, 2007].

Nevertheless, matters are complicated by the fact that volcanic systems show extreme thermal

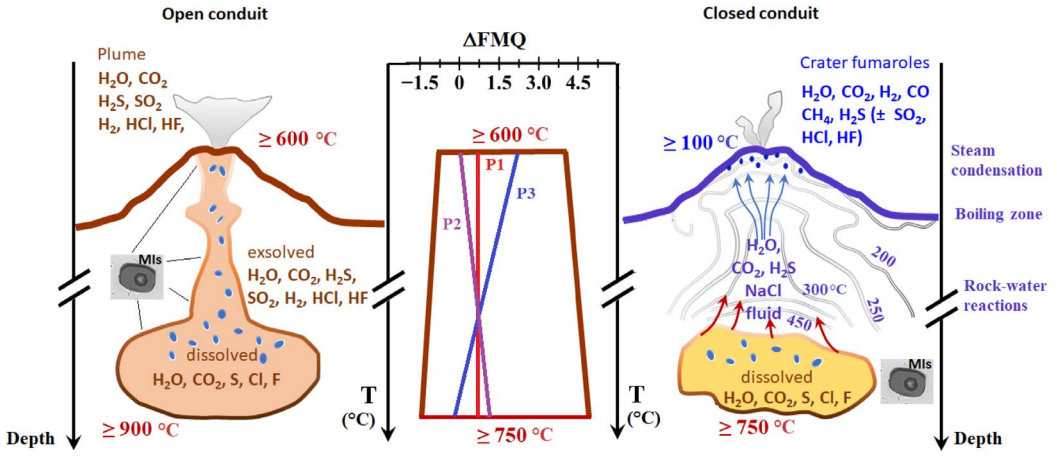

Figure 1. Sketches of open-conduit (left-panel), closed-conduit volcanoes (right-panel), and the range of fO_2 (as ΔQFM) variations of present-Earth magmas (middle panel). Relative fO_2 excursions are from Behrens and Gaillard [2006] for bottom magma ($-1.5 \leq$ QFM ≤ 5) and from the volcanic gas compilation of Moussallam et al. [2019] for the magmatic top (ideally vent conditions for open-conduit volcanoes or shallow magma chamber roofs for closed-conduit volcanoes). P1–P3 are qualitative trends for fO_2 variations throughout volcano plumbing systems. Redrawn and modified from Moretti and Stefansson [2020].

and physiochemical variations from deep regions of magma storage to surface, which are related to polybaric magma crystallization and mixing, as well as to processes of fluid loss/gain, or again rock assimilation [Moretti and Stefansson, 2020, and references therein]. Over the range of temperatures of geological interest for volcanic systems, oxygen fugacity embraces several orders of magnitude (Figure 1). If we embody temperature changes by referring to the same equilibrium mineral assemblage [e.g. Fayalite-Magnetite-Quartz, FMQ; Frost, 1991 and references therein], the ensemble of magmatic redox states encompasses about six orders of magnitudes on the present Earth [Behrens and Gaillard, 2006].

In open-conduit volcanic settings characteristic for "basaltic" (*sensu lato*) magmatism, the main carrier of reactive oxygen up to the surface is hot iron- and sulphur-rich silicate melt, which is possibly a continuum phase from the depth to the surface. However, compositional changes due to magma differentiation, including degassing, can modify significantly the redox state, hence fO_2, *en route* to the surface (Figure 1), given the fundamental role played by composition on iron and sulfur redox couples [Moretti, 2021, Moretti and Ottonello, 2003b, 2022, Moretti and Stefansson, 2020, Cicconi et al., 2020a]. The physiochemical investigation of melt droplets quenched in growing crystals (glass or melt inclusions, henceforth MIs; Figures 1 and 2) during the polybaric evolution of ascending, emplacing and erupting magmas is the basic and most reliable tool to reconstruct the evolution of the fluid phase interacting with the magma from depth up to the crater vents. A large part of the current physiochemical knowledge of volcanic systems, including the main depths of magma storage, comes from magma thermo-oxy-barometry based on the chemical analysis of MIs.

Besides, hydrothermal systems can develop in case of closed-conduit volcanic systems (Figure 1), andesitic *sensu lato*, which are those most prone to violent explosive eruptions. At these volcanoes during periods of quiescence or of pre-eruptive unrest, closed conduit conditions help to accommodate and stabilize magma-induced thermal, baric and chemical anomalies in the form of convective geothermal systems. However, these are also a screen to the deeper magmatic system and its redox signature, deeply modified by the scrubbing of volcanic gases interacting with the aqueous fluids and by the

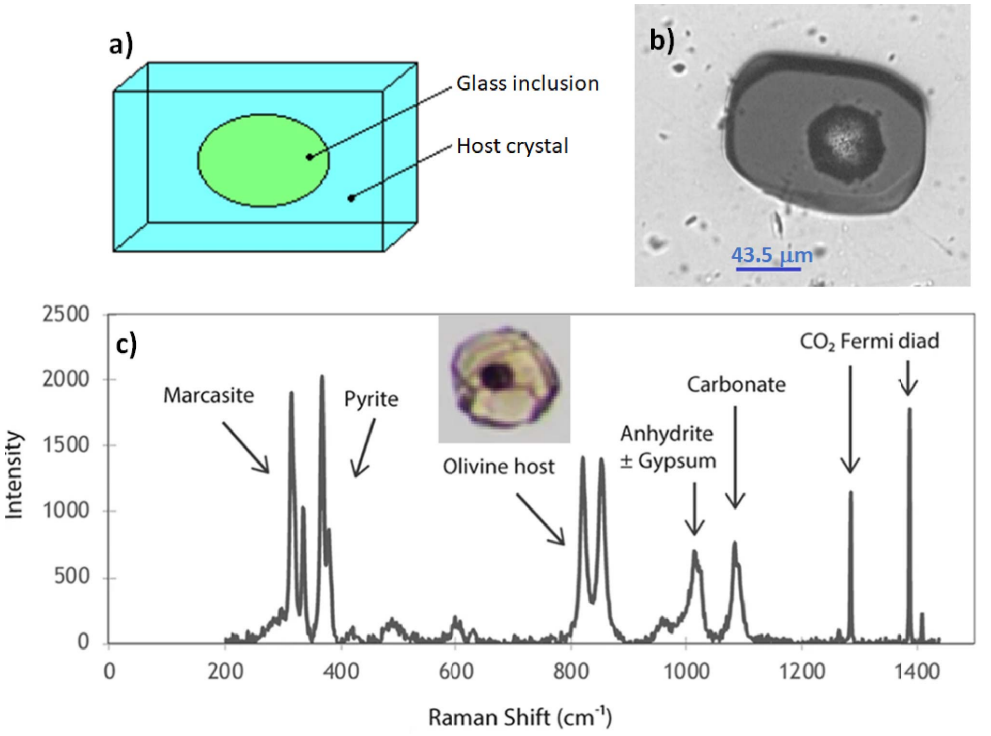

Figure 2. Sketch of a melt inclusion (MI) hosted in a crystal (panel a) and transmission light photograph of an Etna MI carrying a shrinkage bubble (panel b). Raman spectrum (panel c) of the bubble inside a Mt. Meager MI (see insert) carrying a shrinkage bubble and evidences of post-entrapment crystallization. The bubble contains gaseous CO_2, pyrrhotite or pyrite (with polymorphs of marcasite), anhydrite, gypsum, and carbonate (modified from Figure 4 in [Venugopal et al., 2020], under a Creative Commons Attribution 4.0 International license, http://creativecommons.org/licenses/by/4.0/).

subsequent rock–water interaction, and steam separation/condensation processes that are a prelude to fumarolic emissions [Giggenbach, 1987, Hedenquist and Lowenstern, 1994, Moretti and Stefansson, 2020 and Figure 1]. The main geochemical objectives for tracking magma evolution and dynamics in geothermal settings then become the filtering out all these post-magmatic effects from measured fumarolic gases, in order to obtain the pristine magmatic gas getting injected at shallow depths into hydrothermal systems [Caliro et al., 2007, Moretti et al., 2013b]. Again, the analysis of MIs from minerals in magmatic rocks from past eruptions at such settings are fundamental to estimate the compositional variations of the magmatic fluid phase that feeds hydrothermal systems and, thus, to appreciate the current state of many subterranean magma chambers [Arienzo et al., 2010, Moretti et al., 2013b]. More importantly, thermo-oxy-barometric studies of MIs may help in putting constraints about fluid-magma thresholds for reactivation, migration and destabilization of the magmatic chamber(s) below the hydrothermal body, with obvious implications for the assessment of the hazard related to explosive volcanic activity [e.g., Boichu et al., 2008, 2011, Tramontano et al., 2017, Moretti et al., 2019].

The access to a correct thermo-oxy-barometric information on a volcanic system then depends largely on (1) the availability and conditions of occurrence of MIs, (2) their successful analysis and (3) the used equations, which in turn result from calibrations on experimental data and their quality.

In this contribution, after a description of the state of the art about MIs and of main modelling issues of their volatile contents, we will set a parametric comparison of main oxybarometers available in the

literature. We will also provide a brief overview of the interplay between magma redox and major element chemistry, in order to show the role of composition on redox variations observed in nature. The performances and implications of different models on andesitic and basaltic melts of volcanological interest will be then presented. Finally, an application to volcano Etna will illustrate the role that the highly soluble water component plays by shifting redox equilibria at different moments of magma evolution.

2. Melt inclusions and models of fluid saturation and redox state: a brief summary of the state of the art

2.1. *Generalities*

In igneous rocks, glass or melt inclusions (MIs) are micrometric droplets of quenched melts hosted in crystals such as olivine, clinopyroxene or plagioclase (Figure 2). They provide unique insights into the nature of the magma, such as deep source (e.g., mantle), polybaric storage conditions, magma differentiation driven by magma mixing and/or fractional crystallization, pre-eruptive volatile contents and redox state [e.g., Schiano, 2003, Moretti et al., 2013a, Arienzo et al., 2016]. The measurement of their volatile content has boosted the assessment of volatile budgets of endogenous origin, particularly CO_2, S and halogens [e.g., Metrich and Wallace, 2008, Wallace and Edmonds, 2011]. Pre-existing bubbles already exsolved from a fluid-saturated melt may be trapped inside MIs, but in most cases trapped MIs are saturated monophase melt droplets, decoupled from their vapour phase.

After melt entrapment, MIs may undergo further compositional change due to growth of the host crystal at the expense of the MI rims or crystallization of daughter minerals from the melt/glass in response to slow ascent rates and system cooling [e.g. Venugopal et al., 2020; Figure 2]. Besides, during magma rise and consequent decompression, cooling or post-entrapment crystallisation, dissolved volatiles may diffuse and exsolve, nurturing trapped bubbles (if any) or nucleating into a new one (so called vapour or shrinkage bubble). This results from differential thermal contraction of host crystal and melt, which lowers pressure in the inclusion and generates CO_2 saturation [e.g., Wallace et al., 2015a]. Therefore, an initially undersaturated MI can become saturated. Besides, MI vapour bubbles are reservoirs of major and volatile elements (such as S, H_2O, CO_2, Fe, Ca and Mg) that diffuse from the melt/glass phase to form new phases within the bubble. This diffusion is a source of systematic errors that affect the data obtained from analysis of the sole glassy portions of MIs and thus in turn the estimates of storage parameters (T, P, fO_2) [Venugopal et al., 2020, and references therein].

Major elements plus Cl, F and S can be measured by electron microprobe (EMP). Some other light elements (Li, B, Be) are suitably detected by Secondary Ion Mass Spectrometry (SIMS). SIMS also provides trace element and volatile (e.g., H_2O, S, Cl, F, CO_2) analysis, and sub-per mil precision for a wide variety of light stable isotope ratios, including those of trace-level elements (δD, $\delta^{13}C$, $\delta^{18}O$, $\delta^{34}S$, $\delta^{7}Li$, $\delta^{11}B$, $\delta^{37}Cl$) [e.g., Hauri, 2002, Hauri et al., 2002, Gurenko et al., 2005, Manzini et al., 2017]. Laser ablation inductively coupled plasma mass spectrometry (LA-ICP-MS) is the most well-established method for the determination of trace element abundances in MIs and their host minerals [e.g., Pettke et al., 2004]. Abundance and speciation of dissolved H_2O and CO_2 can be quantified via (transmitted light) micro-Fourier-transform infrared spectroscopy (FTIR) [e.g., Ihinger et al., 1994]. Iron and sulfur oxidation state and speciation can be determined via (synchrotron assisted) X-ray absorption near-edge structure (XANES) spectroscopy at the iron and sulfur K-edges [e.g., Lerner et al., 2021]. Iron oxidation state can also be evaluated via synchrotron assisted-Mossbauer spectroscopy [Gaborieau et al., 2020], as well as via Raman spectroscopy [Le Losq et al., 2019], whereas sulfur oxidation state can be assessed using EMP but at lower levels of precision than S-XANES [Carroll and Rutherford, 1988]. Finally, Raman spectroscopy is routinely used to not only determine water content and speciation [Le Losq et al., 2012, 2013], but also to identify and estimate the CO_2 present in the bubble and reveal the presence of mineral precipitates in the bubble, such as carbonates, other solid phases sequestering sulfur and also H_2O in liquid form or structurally bound to hydrous minerals [Venugopal et al., 2020; Figure 2b].

We refer to the literature for a discussion of challenges, pros and cons of each method (calibration techniques, resolution of matrix effects, sample

preparation, destructive versus non-destructive analyses, photo-oxidation/reduction), which should be carefully addressed for planning melt inclusion studies.

The continuous development of microanalytical techniques suitable for MIs' characterization has boosted a fruitful and virtuous three-way link involving (1) experimental petrology to synthesize volatile-saturated glasses from melts of different compositions quenched at different P–T–fO_2 conditions; (2) thermodynamic modelling of volatile saturation (or mixed solubility) and redox properties of melt–fluid systems, and (3) observational volcanology and analytical geochemistry to provide input data from MIs and gas emissions. Saturation/redox models can then be used as thermo-oxy-barometer to reconstruct magma polybaric evolutions and degassing patterns, including fO_2 evolution from depth to surface (see Figure 1).

2.2. *H_2O–CO_2-melt thermobarometry, degassing style and fluid–melt budgets*

The quest for magmatic H_2O and CO_2 abundances has fostered an impressively vast amount of studies about magma degassing and the identification of depths of reservoir in which magmas pond by using several thermobarometic functions describing volatile solubility [see Papale et al., 2022, for a review]. These functions all have a thermodynamic background and have been used to implement models of gas–melt equilibrium in conjunction with an equation of state for H_2O–CO_2 in the gas phase. The most complete approaches include the full assessment of interaction parameters between oxide components (including H_2O and CO_2) in the melt phase, calibrated on the basis of experimental data about volatile solubility in melt at different pressures, temperatures and compositions relevant to magmas [see Papale et al., 2022, and references therein]. These models are also redox dependent, as the relative proportion of FeO and Fe_2O_3, particularly in iron-rich magmas, can shift significantly the H_2O–CO_2-melt saturation surface [Papale et al., 2006].

Because at depth the magmatic gas phase is essentially made of water and carbon dioxide, the (total) pressure of natural volcanic systems is approximated by the sum of H_2O and CO_2 partial pressures. These models have then done a great job in conceptualizing volcanic plumbing systems by giving a depth to main magma reservoirs, where most host crystals develop and trap MIs. This important information can then be confronted to assessments of geophysical nature from seismic and geodetic investigations [e.g., Mangiacapra et al., 2008, Arienzo et al., 2010]. Additionally, adoption of these models on MI-dissolved volatile contents have allowed to reproduce the polybaric degassing paths within the volcanic plumbing system. These paths are, among others, a function of the total (exsolved plus dissolved, or initial) volatile content: upon degassing, the total content of volatile components is constant in closed systems whereas its decreases in open systems; in both scenarios, H_2O and CO_2 partition differently between the melt and gas phases at any pressure step [Papale et al., 2006]. The distributions of MIs' dissolved volatile contents from many volcanic sites show in particular that maximum dissolved CO_2 contents measured in MIs cannot be reconciled with degassing patterns, demonstrating that a significant CO_2-rich exsolved fluid phase exists at depth [e.g., Spilliaert et al., 2006, Aiuppa et al., 2007, 2010, Vigouroux et al., 2008, Allard, 2010, Blundy et al., 2010, Mormone et al., 2011, Oppenheimer et al., 2011, Pino et al., 2011, Moretti et al., 2013a,b, 2018, 2019, Hartley et al., 2014, Caricchi et al., 2018, Paonita et al., 2021]. This evidences that CO_2 dissolved in deep melts significantly underestimates the total CO_2 content, which is in line with the clear imbalance between magma production (magma emitted at the surface and piled up in volcanic edifices) and degassing rates at many volcanic sites, which in turn implies deep degassing sources [e.g., Aiuppa et al., 2007, 2011, 2013, Shinohara, 2008, Moretti et al., 2013a,b, Paonita et al., 2021, Pistone et al., 2021, Utami et al., 2021].

2.3. *Redox-oxygen fugacity models for melts/glasses*

Carmichael [1966] and Carmichael and Nicholls [1967] used the oxy-thermometer of Buddington and Lindsley [1964] based on the two iron-titanium oxide solid solutions titanomagnetite (Fe_3O_4–Fe_2TiO_4) and hemoilmenite (Fe_2O_3–$FeTiO_3$) to bracket fO_2–T ranges of basaltic and acidic volcanic rocks. They showed that the fO_2 of most of the glassy rocks, rapidly quenched and not affected by subsequent cooling, were quite close to the FMQ buffer. Since

then, a scientific debate was initiated on the preservation (and the role) of the deep fO_2 source signature in shallow magma, erupted products and discharged plume gases: was the fO_2 of the rising magma maintained constant, or undergoing either reduction or oxidation (P1, P2 and P3, respectively, in Figure 1).

Besides, interest grew around general formulations relating fO_2 and melt oxidation state, which started to be widely investigated by experimental petrology. In a suite of papers in the 1980s and early 1990s Carmichael and coworkers expounded their well-known composition-dependent equation relating iron oxidation state and fO_2 in melts/glasses, calibrated on a large amount of experimental data [Kress and Carmichael, 1991, and references therein]. This equation became the reference to calculate the fO_2 of magmas, provided an estimate of Fe^{III}/Fe^{II} was available. Reference iron oxidation values were taken from whole rock analyses or alternatively were calculated by the olivine–melt [Roeder and Emslie, 1970] or Cr-spinel–olivine [Maurel and Maurel, 1982] exchange coefficients of Fe and Mg, provided the total iron content from EMP analyses of glass (matrix or inclusions) in contact with these minerals was available. The latter two are reliable techniques as long as melt–mineral equilibrium can be assumed, a condition which in polybaric volcanic rocks is most often satisfied for more primitive specimens slowly equilibrated in deep reservoirs. For example, by using the Roeder and Emslie [1970] and Maurel and Maurel [1982] functions on analyses of deep samples from Ischia and Aeolian island, D'Antonio et al. [2013] could show two trends for Italian volcanic rocks: (1) recent southern Italy volcanics show net increasing oxidation with increasing K-content, associated with the abundance of subduction-derived hydrous fluids, whereas (2) older potassic to ultrapotassic magmas of central Italy display a gentle reduction with increasing K-content, associated with CO_2-dominated conditions likely due to carbonate assimilation.

The possibility offered by modern probes and spectroscopic tools to measure directly the oxidation state of redox sensitive elements (mainly iron and sulfur) in glasses has triggered the interest for formulation of new oxybarometers based on Fe- and S-oxidation states and which were used to show that oxygen fugacity of deep-seated, mantle-derived, melts can be strongly affected by the degassing of volatiles during magma ascent to the surface (qualitative paths P2 and P3 in Figure 1). By adopting modern probes on a set of melt inclusions, in conjunction with the measurement of the composition of volcanic plume gases, it is now possible to model volcanic fluid speciation from depth to surface. This is achieved by separating the contribution of fO_2 due to the deep source's compositional features, from those of the subsequent magma differentiation, the degassing style and also the cooling. Nevertheless, the results will depend on the functional forms adopted for both fluid–melt saturation and oxygen fugacity.

2.3.1. *Iron oxybarometers*

The starting point is the melt oxide component reaction:

$$FeO_{1.5(melt)} \Leftrightarrow FeO_{(melt)} + 1/4O_2 \tag{1}$$

in which $FeO_{1.5}$ replaces conveniently Fe_2O_3. By introducing the activity coefficients γ_{FeO} and $\gamma_{FeO_{1.5}}$ its equilibrium constant takes the form:

$$\begin{aligned} \log K_1 &= \log \frac{a_{FeO_{melt}}}{a_{FeO_{1.5,melt}}} + \frac{1}{4}\log \frac{f_{O_2}}{f^0_{O_2}} \\ &= \log \frac{\gamma_{FeO_{melt}}}{\gamma_{FeO_{1.5,melt}}} + \log \frac{X_{Fe^{II}_{melt}}}{X_{Fe^{III}_{melt}}} + \frac{1}{4}\log \frac{f_{O_2}}{f^0_{O_2}} \end{aligned} \tag{2}$$

with $f^0_{O_2} = 1$ bar (standard state at 1 bar, T of interest).

From (2) we immediately deduce that the parameterization of $\gamma_{FeO_{melt}}/\gamma_{FeO_{1.5,melt}}$ is the key to obtain successful formulation to relate iron oxidation state to oxygen fugacity.

Jayasuriya et al. [2004] based their formulation starting from the adoption of a symmetric regular solution mixing model [see also Moretti and Ottonello, 2022] to solve equation:

$$\begin{aligned} \ln \frac{\gamma_{FeO_{1.5}}}{\gamma_{FeO}} &= \frac{\sum_j^n X_j (W_{FeO_{1.5}-j} - W_{FeO-j})}{RT} \\ &\quad - \frac{(X_{FeO_{1.5}} - X_{FeO}) W_{FeO-FeO_{1.5}}}{RT} \end{aligned} \tag{3}$$

with $W_{FeO_{1.5}-j}$ and $-W_{FeO-j}$ interaction parameters between $FeO_{1.5}$ (or FeO) with the jth oxide melt component. With some simplifications requiring calibration of empirical coefficients, they rework

(3) into the following composition-dependent relation:

$$\ln\frac{X_{\mathrm{Fe^{III}_{melt}}}}{X_{\mathrm{Fe^{II}_{melt}}}} = \frac{a}{T} + b + \sum_i c_i X_i + d\frac{(X_{\mathrm{FeO_{1.5}}} - X_{\mathrm{FeO}})}{T} + \frac{1}{4}\ln f_{\mathrm{O_2}} \quad (4)$$

with a, b, c_i and d coefficients calibrated over the available experimental database on iron oxidation state in silicate glasses (we refer to the original work for the values of coefficients). Equation (4) (henceforth *Jay*) is valid at 1 bar and does not account for the role of volatile components, particularly the light and highly soluble water component.

The search for one general formulation for all melt compositions of geological interest led the authors to formulate empirical expressions based on adjustable parameters, with even less formal rigor than (4). Among these we can recall the expressions from Carmichael and coworkers [Kress and Carmichael, 1991, and references therein] and the Borisov et al. [2018] one (henceforth *Bo*), which use expressions of the type:

$$\ln\frac{X_{\mathrm{Fe^{III}_{melt}}}}{X_{\mathrm{Fe^{II}_{melt}}}} = \frac{a}{T} + b + \sum_i c_i X_i + d\cdot\ln f\mathrm{O_2} \quad (5)$$

with a, b, c_i and d being coefficients that are again calibrated on a vast database, essentially at 1 bar (again we refer to original works for coefficient values). The complete version of the Kress and Carmichael [1991] equation (henceforth *K&C*) includes however the effect of pressure and water and takes the form

$$\ln\frac{X_{\mathrm{Fe_2O_{3,melt}}}}{X_{\mathrm{FeO_{melt}}}} = a\ln f_{\mathrm{O_2}} + \frac{b}{T} + c + \sum_i d_i X_i + e\left[1 - \frac{T_0}{T} - \ln\frac{T_0}{T}\right] + f\frac{P}{T} + g\frac{(T-T_0)P}{T} + \frac{P^2}{T} \quad (6)$$

with P in Pascal, T in K, T_0 = 1673 K and a, b, c_i and d the calibrated coefficients. Note that (6) returns $X_{\mathrm{Fe_2O_{3,melt}}}/X_{\mathrm{FeO_{melt}}}$ instead of $X_{\mathrm{Fe^{III}_{melt}}}/X_{\mathrm{Fe^{II}_{melt}}}$.

Equation such as (5) and (6) violate reaction (1) stoichiometry (i.e., $d \neq 1/4$ in (5) and the same for a in (6)), which implies the loss of internal consistency and the failure of the Gibbs–Duhem relation for all component activities within the same phase [e.g., Lewis and Randall, 1961]. Besides, this alteration of the O_2 stoichiometric coefficient disagrees with mass conservation requirements of reaction (1). Equations of the type (6) do the job of fitting the iron oxidation state in multicomponent systems, only within the compositional domain in which they have been calibrated but they cannot be used to model the iron oxidation state in alkali-rich melts, particularly silica–alkali oxide binaries. However, multicomponent melts of geological interest tend to average the distribution of the effective charge of the oxygen ligand and and surrounding metals [see Ottonello et al., 2001, Moretti, 2005, 2021, Moretti and Ottonello, 2022, for extensive discussion].

To put it in ionic form, by introducing the oxide ion, O^{2-}, we may intuitively rewrite (1) as:

$$\mathrm{Fe^{3+}} + 1/2\mathrm{O^{2-}} \Leftrightarrow \mathrm{Fe^{2+}} + 1/4\mathrm{O_2} \quad (7)$$

From (7), at constant temperature and oxygen fugacity (e.g. on air, $f\mathrm{O_2} = 0.21$), we expect that alkali addition and consequent increase of O^{2-} activity should favour the reduced form of iron, Fe^{2+}. However, the opposite is observed: iron oxidation occurs, as is well known in the industrial glass practice dealing with silica–alkali binaries [e.g., Paul and Douglas, 1965]. Given this evidence, from (2), the $\gamma_{\mathrm{FeO_{melt}}}/\gamma_{\mathrm{FeO_{1.5,melt}}}$ ratio should then increase by an amount equal to the $X_{\mathrm{Fe^{II}_{melt}}}/X_{\mathrm{Fe^{III}_{melt}}}$ decrease in order to keep $\log K_1$ equation (2) constant at the fixed P, T, and $f\mathrm{O_2}$ conditions ($\log K_1$).

However, if we compare the equilibrium constants of reactions (1) and (7) we obtain:

$$\log\frac{\gamma_{\mathrm{FeO_{melt}}}}{\gamma_{\mathrm{FeO_{1.5,melt}}}} = \log K_6 - \log K_1 - \frac{1}{2}\log[\mathrm{O^{2-}}] \quad (8)$$

(square brackets denoting ion activity) which tell us that the increase of oxidation following $[O^{2-}]$ increase on alkali addition should instead determine a counterintuitive decrease of the $\gamma_{\mathrm{FeO_{melt}}}/\gamma_{\mathrm{FeO_{1.5,melt}}}$ ratio.

This behavior, which implies maxima and minima in the activity ratio variation with composition even on a simple binary, cannot be formalized by means of regular or sub-regular mixing models of melt oxide components and their expansion in several terms. Rather, this behavior implies a change of trivalent iron speciation:

$$\mathrm{Fe^{III}O_4^{5-}} \Leftrightarrow \mathrm{Fe^{2+}} + 7/2\mathrm{O^{2-}} + 1/4\mathrm{O_2} \quad (9)$$

Contrary to reaction (7), this reaction has O^2-terms on its (oxidized) left-side.

By comparing K_1, Equation (2) and K_9 we then obtain:

$$\log \frac{\gamma_{FeO_{melt}}}{\gamma_{FeO_{1.5,melt}}} = \log K_9 - \log K_1 + \frac{7}{2}\log[O^{2-}] \quad (10)$$

which demands increasing $\gamma_{FeO_{melt}}/\gamma_{FeO_{1.5,melt}}$ for increasing $[O^{2-}]$ and increasing iron oxidation.

Trivalent iron has then a dual (or amphoteric) behavior (either network modifier, as Fe^{3+}, or former, as $Fe^{III}O_4^5$; [Ottonello et al., 2001, Moretti, 2005, 2021, Le Losq et al., 2020, Moretti and Ottonello, 2022] that implies the concomitance of two ionic redox couples (reactions (7) and (9)) which results from the combination of ion half-reactions (or iron redox elecrodes):

$$Fe^{3+} + e^- \Leftrightarrow Fe^{2+} \quad (11)$$

$$Fe^{III}O_4^{5-} + e^- \Leftrightarrow Fe^{2+} + 4O^{2-} \quad (12)$$

with the so-called oxygen electrode [Ottonello et al., 2001, Moretti, 2005, Cicconi et al., 2020b, Moretti and Neuville, 2021, Moretti and Ottonello, 2022]:

$$1/4O_2 + e^- \Leftrightarrow 1/2O^{2-} \quad (13)$$

In the so-called ionic-polymeric approach (henceforth *IPA*), Ottonello et al. [2001] and Moretti [2005] consider this dual behavior of iron in melts and by rewriting $Fe^{III}O_4^{5-}$ as $Fe^{III}O_2^-$ [following Fraser, 1975] they set a composition-dependent model that defines the activity of oxide ions, $[O^{2-}]$, or activity of "free oxygen" [also called non-network associated oxygen; Nesbitt et al., 2011]. By distinguishing between a cationic matrix (made of network modifiers) and an anionic matrix [made of oxyanions or *structons*, in the sense of Fraser, 1975], like in the Temkin model for fused salts [Temkin, 1945] the activity of the generic MO oxide (M being a metal) is given by the product of its ion activities:

$$\begin{aligned} a_{MO(Temkin)} &= a_{M^{2+}} a_{O^{2-}} = x_{M^{2+}} x_{O^{2-}} \\ &= \frac{n_{M^{2+}}}{\sum \text{cations}} \cdot \frac{n_{O^{2-}}}{\sum \text{anions}} = \frac{n_{M^{2+}}}{\sum \text{cations}} \\ &\cdot \frac{n_{O^{2-}}}{\sum \text{structons} + \sum \text{"free"anions} + n_{O^{2-}}} \end{aligned} \quad (14)$$

with free anions being represented by anions such as S^{2-}, SO_4^{2-}, Cl^- but also OH^- groups (free hydroxyls) that are not covalently linked to the melt network to form T–OH groups (T being a network former) [Moretti et al., 2014, and references therein].

Structons are the polymeric entities making up the network and thus expressing the reactivity of the oxygen ligand. They are computed [see Moretti, 2005, for details] by accounting for melt polymerization, which is the partitioning of melt–oxygen in three forms [Toop and Samis, 1962b,a]

$$O^0 + O^{2-} \Leftrightarrow 2O^- \quad (15)$$

with O^0, O^{2-} and O^- representing, respectively, bridging oxygen, free oxygen (or non-network associated oxygen or oxide ion) and non-bridging oxygen. Their mixing, formalized by the polymerization constant K_{15}, is the key to understanding melt mixing properties and reproducing correctly the *V*-shaped form of the Gibbs free energy of mixing and then the component activites [Ottonello, 2001, 2021, Ottonello et al., 2001, Ottonello and Moretti, 2004].

Because of their large thermal stability and their nature of continuous oxygen network, silicate melts are solutions that change their polymerization properties, and hence the network topology, while dissolving important amounts of other metals. Basically this means that, contrary to aqueous solutions, the distinction between solvent (the oxygen ligand structured in the melt network) and solute becomes blurred, without the possibility of defining and distinguishing solvation shells within which covalent bonding forces are exhausted [Moretti and Neuville, 2021, Moretti and Ottonello, 2022]. So, every added component impacts on the structure via polymerization, affecting the (undistinguished) solvent and solute. For example, water has a well-known large P-dependent solubility which results from breaking the biggest network units and melt depolymerization [see Papale et al., 2022, for a review].

Polymerization equilibrium K_{15} then shifts with composition because any silicate network is a solvent *per se* with peculiar dielectric and electrostriction properties, hence with a specific structural framework whose polymerization is the main chemical descriptor. Because of this, the continuous shift of polymerization with composition impacts the redox equilibrium in a non-linear way via its effect on $[O^{2-}]$ and also terms that are mainly entropic about component relaxation in melts [Ottonello, 2021, Moretti and Ottonello, 2003a, Ottonello, 2005, Moretti, 2021]. In fact, depending on bulk composition, K_{15} involves a change in the oxidation state of oxygen and hence

in the polarization state of the ligand and in network relaxation [Ottonello et al., 2001, Moretti, 2005]. Because the shift in the ligand polarization state affecting the network reactivity is related to the ionic (or covalent) bond fraction, and thus to atomistic properties, such as electronegativity or optical basicity [Duffy, 1993, Moretti and Ottonello, 2022, and references therein], Ottonello et al. [2001] proposed a composition-dependent polymerization constant based on the contrast in atomistic properties (optical basicity) between the anionic and the cationic matrix.

The *IPA* considers then dissociations of iron oxides into their ionic products:

$$FeO \Leftrightarrow Fe^{2+} + O^{2-} \tag{16}$$

$$Fe_2O_3 \Leftrightarrow 2Fe^{3+} + 3O^{2-} \tag{17}$$

$$Fe_2O_3 + O^{2-} \Leftrightarrow 2Fe^{III}O_2^- \tag{18}$$

The final iron redox equation embodies then the amphoteric role of trivalent iron depending on composition via the parameterization of $[O^{2-}]$, Σ anions and Σ cations:

$$\frac{Fe^{III}}{Fe^{II}} = \frac{N_{Fe^{III}}}{N_{Fe^{II}}} = \frac{[FeO_2^-]\sum \text{anions} + [Fe^{3+}]\sum \text{cations}}{[Fe^{2+}]\sum \text{cations}} = \frac{f_{O_2}^{1/4}}{K_1} \cdot \frac{K_{18}^{1/2}[O^{2-}]^2\sum \text{anions} + K_{17}^{1/2}\sum \text{cations}}{[O^{2-}]^{1/2}K_{16}\sum \text{cations}} \tag{19}$$

in which the last fractional term on the right corresponds to $\gamma_{FeO_{melt}}/\gamma_{FeO_{1.5,melt}}$ in (2).

Based on literature data on iron oxidation state, the *IPA* parameterizes K_1, K_{16}, K_{17} and K_{18} [Ottonello et al., 2001] and it was further expanded at pressure including volume terms for ionic species and oxide components by evaluating $\int \Delta V_{reaction}\,dP$ terms for each reaction, as well as water speciation [Moretti, 2005, Moretti et al., 2014].

Moretti and Ottonello [2022] presented ab-initio implicit calculation of iron redox in melts. In their approach, based on Tomasi's Polarized Continuum Model [PCM; Floris and Tomasi, 1989, Floris et al., 1991, Tomasi and Persico, 1994, Tomasi et al., 1999], there is no need to consider the structure of the silicate framework, because medium properties are summarized in its dielectric properties. Results (for the moment at 1 bar and 25 °C) confirm the role of the two redox reactions (7) and (9), as well as of the oxygen electrode reaction (13).

2.3.2. *Sulfur oxybarometers*

In a silicate melt, it is generally assumed that the most abundant S-species are sulfide and sulfate ions and sulfur dissolution in melt is expressed as [Fincham and Richardson, 1954, Sakai et al., 1982, Wallace and Carmichael, 1992, 1994, Carroll and Webster, 1994, Moretti et al., 2003, Moretti and Ottonello, 2003a, 2005, Baker and Moretti, 2011, Nash et al., 2019]:

$$S_{2(g)} + 3/2O_2 + O^{2-} \Leftrightarrow SO_4^{2-} \tag{20}$$

$$S_{2(g)} + O^{2-} \Leftrightarrow S^{2-} + 1/2O_2 \tag{21}$$

Reactions (1) and (2) are at the core of the definition of so-called sulfate and sulfide capacities:

$$C_{S^{6+}} = [S]_{wt\%} f_{O_2}^{-3/2} f_{S_2}^{-1/2} \tag{22}$$

$$C_{S^{2-}} = [S]_{wt\%} \left(\frac{f_{O_2}}{f_{S_2}}\right)^{1/2} \tag{23}$$

which are related to equilibrium constants of reactions (20) and (21) and represent a peculiar quantity of any melt of given composition.

By subtracting reaction (21) from reaction (20), the typical redox mechanism for sulfur dissolved in melts (also undersaturated ones) can be obtained:

$$S^{2-} + 2O_2 \Leftrightarrow SO_4^{2-} \tag{24}$$

Because of the absence of O^{2-} terms, reaction (24) may appear to be independent of melt composition and be ruled only by temperature and oxygen fugacity, fO_2. Nevertheless, the partitioning of dissolved sulfur between sulfide (S^{2-}) and sulfate (SO_4^{2-}) depends on composition, like in the dissolution reactions (20) and (21) [Klimm et al., 2012], because of the composition-dependent interplay of sulfide and sulfate ions with cations and also with the S-free melt network [Moretti and Ottonello, 2005, Moretti, 2021, and references therein; see also Papale et al., 2022].

The redox numerical model, Conjugated Toop-Samis-Flood-Grjotheim (CTSFG) model, solves for the sulfide and sulfate capacities of any melt composition based on a linear combination of the equilibrium constants of the type of (20) and (21) for single oxide–sulfide and oxide–sulfate pairs and considering that:

$$C_{S,c} = K'_{O-S,M}(O^{2-}) \left(\frac{f^0O_2}{f^0S_2}\right)^{1/2} M_S \sum_{mol} \text{oxides} \tag{25}$$

with (O^{2-}) the "free oxygen" amount, Σ_{mol} oxides the molar summation of all oxides in the system on a

percent basis, M_S atomic weight of sulfur, f^0O_2 and f^0S_2 the standard state fugacities of gaseous components (1 bar) and $K'_{O–S,M}$ the combined equilibrium constant ((20) for sulfide, (21) for sulfate) resulting from the combination of single oxide–sulfide or oxide–sulfate pairs [Moretti and Ottonello, 2003a, 2005].

The Moretti and Ottonello [2005] CTSFG model (see Code Availability section) is calibrated on >1000 experimental data on sulfide and sulfate solubility and allows estimating the amount of sulfur dissolved in melts as:

$$\begin{aligned}[S]_{wt\%,tot} &= [S]_{wt\%,sulfide} + [S]_{wt\%,sulfate} \\ &= C_{S^{2-}} f S_2^{1/2} / f O_2^{1/2} + C_{S^{6+}} f O_2^{3/2} f S_2^{1/2}\end{aligned} \quad (26)$$

Sulfur oxidation state and speciation is instead independent of fS_2 and calculated as:

$$\frac{S^{6+}}{S_{tot}} = \frac{X_{S^{6+}}}{X_{S_{tot}}} = \frac{C_{S^{6+}}}{C_{S^{6+}} + C_{S^{2-}} f O_2^{-2}} \quad (27)$$

which embodies compositional dependencies via the definition of sulfide and sulfate capacities.

Via the CTSFG model, the *IPA* solves internally the mutual interactions of iron and sulfur species, represented by the equilibria:

$$8Fe^{3+\cdot} + S^{2-} + 4O^{2-} \Leftrightarrow 8Fe^{2+} + SO_4^{2-} \quad (28)$$

$$8FeO_4^{5-\cdot} + S^{2-} \Leftrightarrow 8Fe^{2+} + SO_4^{2-} + 28O^{2-} \quad (29)$$

that can be obtained by summing up reactions (24) and (7), and reactions (24) and (9), respectively [Moretti and Ottonello, 2003b, 2022, Moretti and Papale, 2004]. Reactions (28) and (29) remind us that iron redox couples (exchanging on electron) may accommodate large fO_2 variations via small Fe^{III}/Fe_{tot} variations. Given also iron abundance in natural melts, iron redox couples may be effective buffers of magma redox state. On the other hand, the sulfur redox couple (exchanging eight electrons) experiences large variations for small fO_2 variations that occur typically around FMQ and Nickel–Nickel Oxide (NNO) gas–solid buffers [Frost, 1991, and references therein]. The (composition-dependent) equilibrium constant of reaction (24) can thus be turned into a precise oxybarometer for fO_2 variations embracing FMQ and NNO.

On more empirical grounds, Wallace and Carmichael [1994] proposed the following equation (henceforth *W&C*) linking the mole fractions of SO_4^{2-} (or of S^{6+}) and S^{2-} to redox conditions in the silicate melt:

$$\log(X_{SO_4^{2-}} / X_S^{2-}) = 1.02 \log f O_2 + 25{,}410/T - 10 \quad (30)$$

Similar to the Kress and Carmichael [1991] equation for iron oxidation state, Equation (30) alters the $\log fO_2$ coefficient required by reaction (24) stoichiometry (i.e., 2). Because (30) is actually the equilibrium constant of the redox exchange intervening between reduced and oxidized forms of melt sulfur, the value of ≈1 instead of 2 implies a redox exchange involving one O_2 and thus four electrons rather than the eight that are implicit in reaction (24) to convert S^{2-} into $S^{VI}O_4^{2-}$.

Other simple equations relating the redox state of silicate melts to XSO_4^2 have been also suggested by Wallace and Carmichael [1992], Matthews et al. [1999], Jugo and Luth [2005], and Jugo et al. [2010]. The latter expression (henceforth *Ju*) was calibrated on data from X-Ray Near Edge Absorption (XANES) spectroscopy and has become very popular to assess fO_2 (as ΔFMQ) from sulfur redox data:

$$\frac{S^{6+}}{S_{tot}} = \frac{1}{1 + 10^{(2.1 - 2\Delta FMQ)}} \quad (31)$$

However, these simple approaches disregard composition and imply that XSO_4^{2-}/XS^{2-} would be a simple function of temperature and oxygen fugacity only.

More recently, Nash et al. [2019] proposed an assessment of melt reaction:

$$FeS + 8FeO_{1.5} \Leftrightarrow 8FeO + FeSO_4 \quad (32)$$

The authors considered that the equilibrium of reaction (32), K_{32}, is unaffected by compositional melt variations, and by using thermodynamic data for solid phases they proposed the following oxybarometer (henceforth *NSW*) for Fe–S iron mutual interactions:

$$\log \frac{X_{SO_4^{2-}}}{X_{S^{2-}}} = 8 \log \frac{X_{Fe^{III}}}{X_{Fe^{II}}} + \frac{8.7436 \times 10^6}{T^2} - \frac{27{,}703}{T} + 20.273 \quad (33)$$

Following the authors, the Fe^{III}/Fe^{II} ratio in (33) can be converted to $\log fO_2$ via the *K&C* (6).

3. Comparison of redox models

For the different oxybarometers available in the literature, I model the effect of different proportions of FeO and Fe_2O_3 at a given total iron content (i.e. the

iron oxidation state) on the main redox indicators (fO_2, SO_2/H_2S in gas, S^{VI}/S_{tot} in melt) as well as on saturation pressure and gas H_2O–CO_2 compositions of two different melts of volcanological interests: Soufrière de Guadeloupe andesite [Metcalfe et al., 2022] and Etna basalt [Moretti et al., 2018]. Computations refer to (a) 1 bar and volatile-free conditions (Figure 3) and, for given values of dissolved H_2O–CO_2 from saturated MIs in literature (Table 1), (b) two pressure regimes for each system, represented by dissolved H_2O–CO_2 pairs corresponding to shallow and deep magma reservoirs (Table 1; Figure 4a,b). As independent variable for all computations I take the Fe^{III}/Fe_{tot} ratio, with calculation steps of 0.05. I push the calculation up to 0.99 for the sake of completeness of the present parametric approach, despite Fe^{III}/Fe_{tot} values >0.5 being unrealistic.

In the 1-bar case (Figure 3) I adopted the following oxybarometers: *Bo*, *Jay*, *IPA* and *K&C* for iron redox, and *W&C*, *IPA*, Ju and *NSW* for sulfur redox. In the $P > 1$-bar case (Figure 4) I could not adopt *Bo* and *Jay* for iron redox. Besides, the *IPA* provides a full internal computation of both fO_2 and S-oxidation state, provided the Fe^{III}/Fe_{tot} ratio, whereas *Ju*, *W&C* and *NSW* adopt the fO_2 value from the *K&C* equation, following either explicit model requirements and recommendations [e.g., Wallace and Carmichael, 1994, Nash et al., 2019] or common practices adopted in many studies [e.g., Brounce et al., 2017, Moussallam et al., 2016, Venugopal et al., 2020].

Because in magmatic gases, the prevailing S species are SO_2 and H_2S [e.g., Giggenbach, 1987, Moretti and Stefansson, 2020, and references therein], the following reaction was also included:

$$H_2S + 1.5O_2 \Leftrightarrow SO_2 + H_2O \tag{34}$$

and its equilibrium constant used to calculate the fSO_2/fH_2S ratio ($\approx X_{SO_2}/X_{H_2S}$) via [e.g., Aiuppa et al., 2011]:

$$\log(XSO_2/XH_2S) = 27{,}104/T - 4.113 - \log PH_2O + 1.5\log fO_2 \tag{35}$$

For the dissolved amounts of H_2O and CO_2 measured in MIs in Table 2 [Del Carlo and Pompilio, 2004, Moretti et al., 2018], I used the H_2O–CO_2-melt saturation model of Papale et al. [2006] to evaluate the melt–fluid saturation pressure and the composition of the exsolved gas phase, hence PH_2O in (35).

First of all, the different models return similar oxygen fugacities but with differences which are larger for andesite than basalts and which increase particularly for $Fe^{III}/Fe_{tot} > 0.5$ for both types (Figure 3a,b). The smaller spread of computed values for basalt is likely due to the large presence of basaltic samples in the calibration databases, in large part significantly overlapping for all these functions.

We also see that the *IPA* tends to give the lowest fO_2 values for andesite at $Fe^{III}/Fe_{tot} > 0.2$ but for basalt the *IPA* returns the lowest fO_2s at very oxidized conditions, for $Fe^{III}/Fe_{tot} > 0.8$. The physical limit of $fO_2 = 1$ bar occurs at $Fe^{III}/Fe_{tot} \approx 0.95$ for basalt but at 0.98 for andesite. For basalt, at $Fe^{III}/Fe_{tot} < 0.8$, lowest fO_2 values are returned by the *Jay* model. We can also remark that for andesite highest values are systematically given by the *Bo* model. This model gives also highest values for basalt, but for $Fe^{III}/Fe_{tot} > 0.3$, where it tends to match perfectly the performances of the *K&C* equation. For basalt, at $Fe^{III}/Fe_{tot} < 0.4$, the *Bo* model tends to follow closely the *IPA*, which returns the highest fO_2 values in this range of iron oxidation state. In andesite, for $Fe^{III}/Fe_{tot} < 0.2$, lowest fO_2 values are given by the *K&C* model.

We may also remark that the *Jay* model and the *IPA*, on one side, and the *K&C* and the *Bo* ones, on the other side, have very similar trends and run closely with each other, particularly the *IPA* and *Jay* models in andesite and the *K&C* and *Bo* ones in basalt. This is a consequence of the coefficients for the $\log fO_2$ (or $\ln fO_2$) term, which follows reaction (1) for the *Jay* model and the *IPA*, but which is ≈0.2 for both the *Bo* and *K&C* equations.

In Figure 3b, I also report the fO_2 estimate (−8.44, or ΔFMQ = 0.46) extrapolated at 1150 °C for Etna vents from the relation established by Sato and Moore [1973], even though originally calibrated for temperatures up to 1000 °C:

$$\log fO_2 = 2.175 - 15110/T \tag{36}$$

This value is encountered at Fe^{III}/Fe_{tot} values of 0.17 for *IPA*, 0.18 for *Bo*, 0.2 for *K&C* and 0.24 for *Jay*, resulting in about 35% of dispersion around the mean value (0.198).

The very same behaviors as that of $\log fO_2$ are reported on the log-scale by SO_2/H_2S ratios in Figure 3c,d, as demanded by (35). Worth noting is the range values (20–200) for passive (uneruptive) Etna

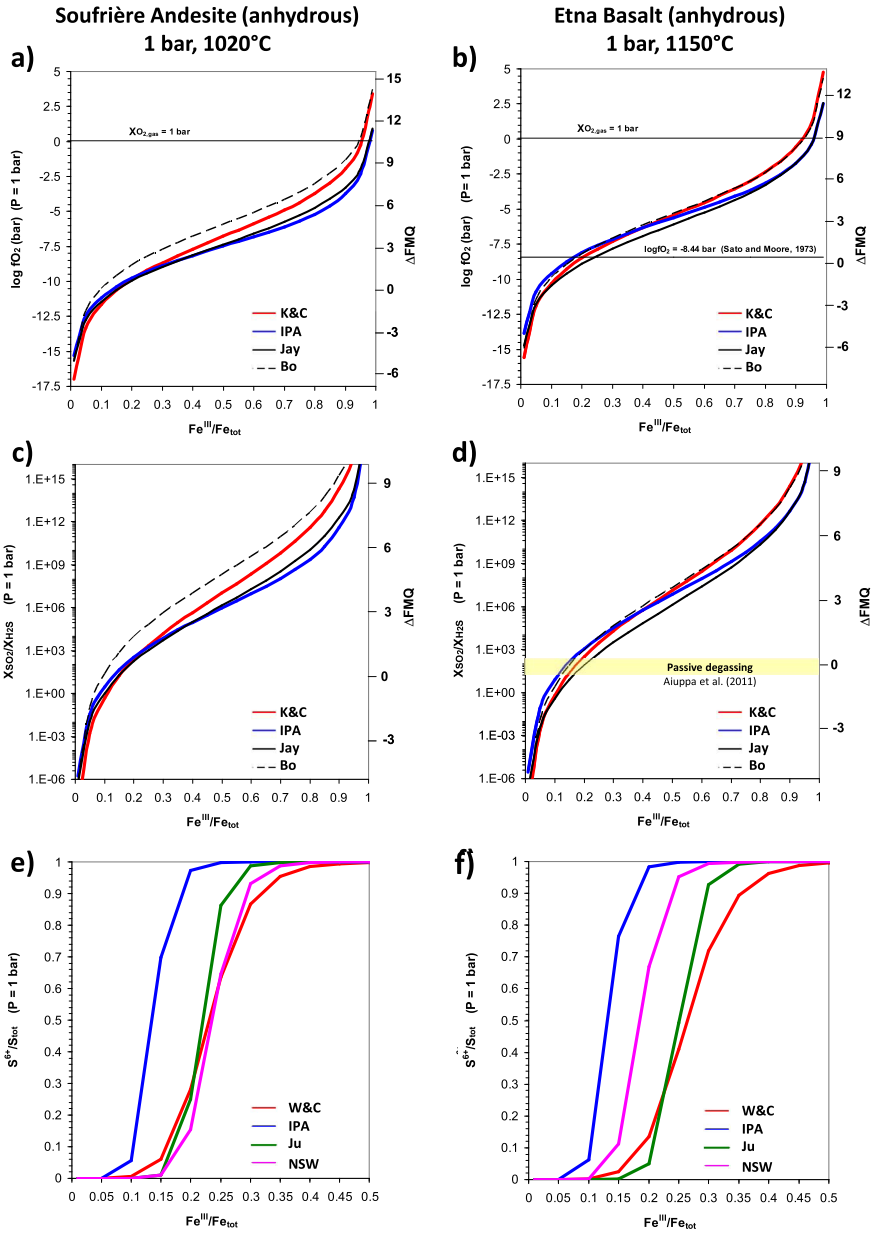

Figure 3. 1-bar computations of $\log fO_2$, SO_2/H_2S and S^{6+}/S_{tot} ratios for varying Fe^{III}/Fe_{tot} ratios via oxybarometers described in this study for a Soufrière de Guadeloupe Andesite at 1120 °C (panels a,c,e) and an Etna basalt at 1150 °C (panels b,d,f). Also reported are the fO_2 value from (36) for Etna vents, extrapolated at 1150 °C (panel b) and the range of SO_2/H_2S variations (20–200) reported for Etna passive degassing (panel d). Right Y-axis in panels a–d refer to relative fO_2 as ΔFMQ; this quantity is not reported in panels e, f because correspondences cannot be unique with S^{6+}/S_{tot} values reported on the primary Y-axis given that the *IPA* and *W&C* use different fO_2 estimations. In this study we attributed fO_2 from the *K&C* equation to the *Ju* and *W&C* models; the *NSW* equation (33) does not use fO_2 explicitly, although Nash et al. [2019] recommend values from the *K&C* equation. See Table 1 for adopted compositions, here simulated as volatile-free.

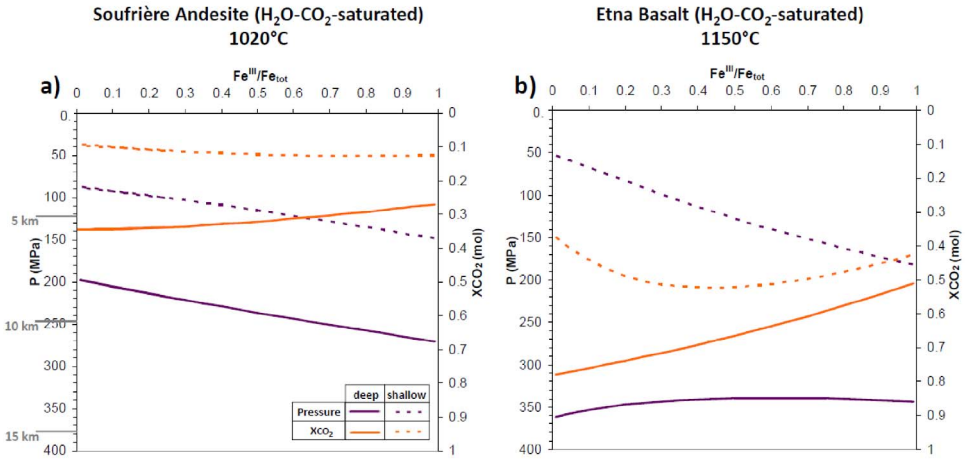

Figure 4. H_2O–CO_2-melt saturation pressures and gas phase composition for the Soufrière andesite at 1020 °C (panel a) and the Etna basalt at 1150 °C (panel b). Solid lines: deep system; dotted lines: shallow system; dark violet: saturation pressure; orange: X_{CO_2} in gas. On the Y-axis are also reported, in grey, three depths (z) computed via $P = \rho g z$, with g the acceleration due to gravity and ρ the magma/rock density, assumed constant at all depths ($\rho = 2500$ kg/m^3).

degassing reported in Aiuppa et al. [2011], which for its upper limit matches the (1-bar) ΔFMQ value of 0.46 from (36). The 20–200 interval (horizontal yellow bar in Figure 3f) is encountered in the ranges 0.11–0.16 for *IPA*, 0.11–0.17 for *Bo*, 0.15–0.19 for *K&C* and 0.17–0.22 for *Jay*. Higher SO_2/H_2S values (say around 1000) should be however expected during pre-eruptive stages, suggesting that the feeding magma arriving at the surface might have larger values of Fe^{III}/Fe_{tot} values, following models' curves in Figure 3d.

S^{6+}/S_{tot} ratios at 1 bar are plotted in Figure 3e,f. In the andesitic case lowest values are returned by the *IPA* (CTSFG model), which is leftward shifted by about 0.1 units in Fe^{III}/Fe_{tot} with respect to the *Ju* model: the *IPA* returns nearly full sulfur oxidation when the *Ju* computes a S^{6+}/S_{tot} ratio of 0.5 at $Fe^{III}/Fe_{tot} \approx 0.22$. Apart from the *IPA*, the *W&C* model gives the most sulfur oxidation for $Fe^{III}/Fe_{tot} < 2$, when it shows a cross-over with the *Ju* model. The cross-over with the *NSW* model is observed at $Fe^{III}/Fe_{tot} \approx 0.25$. Below this value, the *NSW* model returns the highest sulfur reduction. Among these models, the *IPA* and the *Ju* vary from reduced to oxidized in about 0.15 units of Fe^{III}/Fe_{tot}. The *W&C* model varies from fully reduced to fully oxidized in about 0.3 units of Fe^{III}/Fe_{tot}, the *NSW* one in about 0.2 (Figure 3e). The larger Fe^{III}/Fe_{tot} interval displayed by the *W&C* to go from full reduction to full oxidation is related to the $\log fO_2$ coefficient of 1.02 instead of the value of 2 demanded by the O_2 stoichiometric coefficient in reaction (24).

In the basaltic case, the *IPA* curve has trend and variations very similar to the andesitic one, suggesting that T-variations are compensated by compositional differences. Compared to andesite, the *Ju* and *W&C* curves shift to higher Fe^{III}/Fe_{tot}, with slight modifications in their shape due to the different fO_2 for basalt with respect to andesite (provided via the *K&C* equation 6 for both expressions). The *W&C* remains the function requiring the largest Fe^{III}/Fe_{tot} interval to oxidize all sulfide in sulfate.

To describe the redox behavior of H_2O–CO_2-saturated andesite and basalt at given temperatures, we must first investigate the role of iron oxidation state on saturation properties such as pressure and gas phase composition. Figure 4a,b clearly shows the significant impact of iron oxidation state, a fact which is too often disregarded despite the abundance of iron in geological melts. In particular, increasing iron oxidation from fully reduced to fully oxidized decreases saturation pressure by a factor of about two for both "shallow" and "deep" andesite. An even larger variation, by a factor > 3 is observed in "shallow" basalt, whereas "deep" basalt maintains

Table 1. Compositions used in this study

		Soufrière de Guadeloupe andesite	Etna basalt
SiO_2	(wt%)	73.17	47.25
TiO_2	(wt%)	0.537	1.94
Al_2O_3	(wt%)	13.602	16.27
FeO_{tot}	(wt%)	4.48	10.29
MnO	(wt%)	0.126	0.18
MgO	(wt%)	1.053	5.88
CaO	(wt%)	3.558	10.88
Na_2O	(wt%)	1.695	3.5
K_2O	(wt%)	1.653	2.13
T (°C)		1020	1150
Shallow magma			
H_2O	(wt%)	3.4	2.5
CO_2	(ppm by wt)	120	150
P-range (MPa)	100.1–148.6	53.6–182.4	
Deep magma			
H_2O	(wt%)	4.2	3.24
CO_2	(ppm by wt)	866	1833
P-range	(MPa)	197.6–270.5	339.3–361.3
Source		Metcalfe et al. [2022]	Moretti et al. [2018]

Pressure ranges were computed via the Papale et al. [2006] model for Fe^{III}/Fe_{tot} variations from 0.01 to 0.99. The temperature is the equilibrium temperature of the melt + gas system.

values around 350 MPa, even increasing to 365 MPa when approaching full iron reduction. Also, the gas-phase composition shows unexpected behaviors, which appear to depend on pressure: X_{CO_2} increases with increasing Fe^{III}/Fe_{tot} for shallow andesite, but diminishes for the deep one (Figure 4a); in shallow basalt X_{CO_2} shows a minimum at $Fe^{III}/Fe_{tot} \approx 0.45$, whereas in deep basalt X_{CO_2} decreases linearly with increasing iron oxidation.

These results demonstrate that an incorrect estimate of iron oxidation state has obvious implications for geothermobarometry based on melt inclusion volatile contents, resulting in inappropriate petrologic estimates of magma reservoir depths, uncertain reconstruction of plumbing systems and also potentially unacceptable mismatch between petrologic and geophysical observations.

For what concerns fO_2, results are given in Figure 5a,b. The *K&C* model and the *IPA* return nearly the same value under reduced conditions ($Fe^{III}/Fe_{tot} < 1$) for andesite (Figure 5a), whereas for increasing iron oxidation the *K&C* equation returns fO_2 values higher than the IPA, with differences of about 2.5 log-units at the (hypothetical) Fe^{III}/Fe_{tot} value of 0.95, when the *K&C* curve crosses the $fO_2 = 1$ bar line. For andesite, both models compute a fO_2 value slightly higher for shallow magma than deep one for the iron oxidation ratio. In the case of basalt (Figure 5b), the difference in values from the two models are smaller, but the *IPA* gives fO_2 values higher than *K&C* ones for $Fe^{III}/Fe_{tot} < 0.25$. Besides, the *IPA* gives generally fO_2 values that are higher for the deep basalt than for the shallow one and which are up to one-log unit in the 0.01–0.2 Fe^{III}/Fe_{tot} range. On the contrary, $\log fO_2$ values from the *K&C* equation are close for both shallow and deep basalt, but not indistinguishable as for andesite in panel a. The larger spread between deep and shallow basalt (Figure 5b), compared to andesite, is due to the role of pressure–volume terms, which is larger, lower the

Fe^{III}/Fe_{tot} ratio. This effect is greater for the *IPA* than the *K&C* equation.

The $\log fO_2$ value of −8.44 from (36) is encountered by the shallow basalt for iron conditions more slightly reduced than at 1 bar (0.14 and 0.17 in Fe^{III}/Fe_{tot} for the *IPA* and the *K&C* equation, respectively), whereas the deep basalt matches it at slightly more oxidized conditions for both the *K&C* equation ($Fe^{III}/Fe_{tot} = 0.19$) and the *IPA* ($Fe^{III}/Fe_{tot} = 0.23$) (Figure 5b).

As for 1-bar data, log-scale SO_2/H_2S ratios from the *K&C* equation and the *IPA* show the same relative variations of $\log fO_2$ patterns for the same pressure class (deep or shallow; Figure 5c,d). In Figure 5d we see that the 20–200 SO_2/H_2S interval (horizontal yellow bar) reported by Aiuppa et al. [2011] is encountered at Fe^{III}/Fe_{tot} values higher than those from the 1-bar computation, that is, 0.25–0.31 for the *K&C* and the shallow-basalt *IPA*, and 0.31–0.4 for the deep-basalt *IPA*.

S^{6+}/S_{tot} ratios (Figure 5e,f) from the *W&C* and *Ju* equations do not differ substantially from the 1-bar values, differences being related to the role of pressure and dissolved water on the fO_2 calculated via the *K&C* equation. The *NSW* model instead returns the same results as in the 1-bar case, because (33) includes neither pressure nor fO_2 and is P-independent (Figure 5e,f). The most significant variations are displayed by the *IPA* oxybarometer. In the case of andesite, shallow and deep computations are nearly equivalent (the shallow one slightly shifted to higher iron oxidation ratios), but compared to 1-bar results, they are shifted by 0.1 log-units to higher Fe^{III}/Fe_{tot} ratios. In case of basalt, we also observe a shift of 0.05 units to larger Fe^{III}/Fe_{tot} ratios, which become 0.1 for the deep basalt.

4. Application to Etna volcano

Because of its high solubility and pressure-dependence, water is certainly a major component of magmatic differentiation taking place on magma ascent. Therefore, MIs from decompressing and degassing magmas should record the effect of water on iron oxidation state. Figure 6 plots then the MI-based XANES Fe^{III}/Fe_{tot} data reported for Etna basalts in Gennaro et al. [Gennaro et al., 2020; see their Tables 4 and 5] and their covariation with dissolved H_2O content. The data in the figure suggests indeed that the dissolved water can be a major compositional control of iron oxidation at

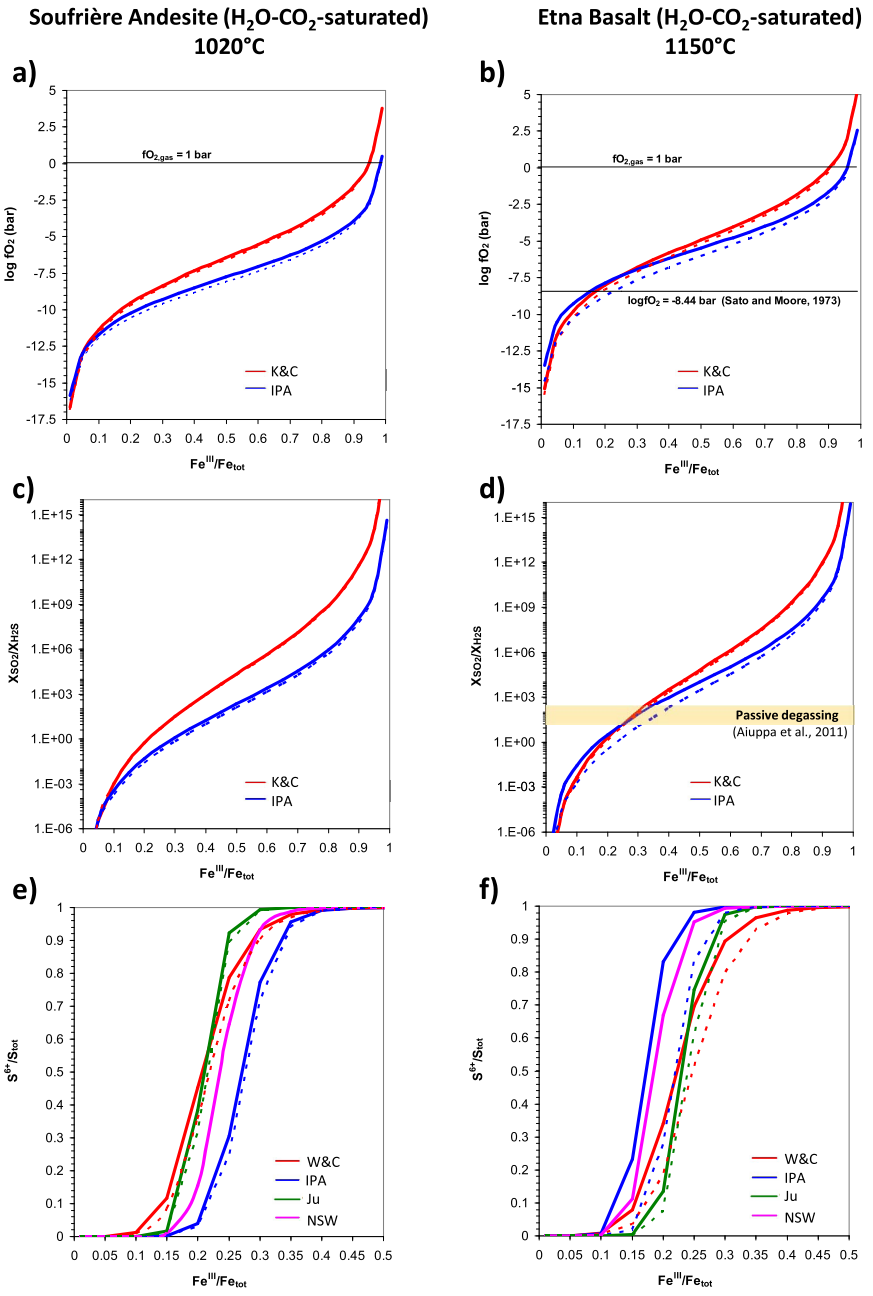

Figure 5. Computations of $\log fO_2$, SO_2/H_2S and S^{6+}/S_{tot} ratios for the same melts as in Figure 4 and for varying Fe^{III}/Fe_{tot} ratios. The different oxybarometers described in this study were adopted. Also reported are the fO_2 value from (36) for Etna vents, extrapolated at 1150 °C (panel b) and the range of SO_2/H_2S variations (20–200) reported for Etna passive degassing (panel d). In all panels, solid lines represent deep magma conditions and dotted lines shallow magma conditions. See Table 1 for adopted compositions. For each computation, corresponding pressure should be read in panels a and b for andesite and basalt, respectively. Because pressure is not constant, contrary to the 1-bar case of Figure 3, relative fO_2 as ΔFQM is not given on secondary Y-axes, given that multiple ΔFQM values would correspond to quantities reported on primary Y-axes.

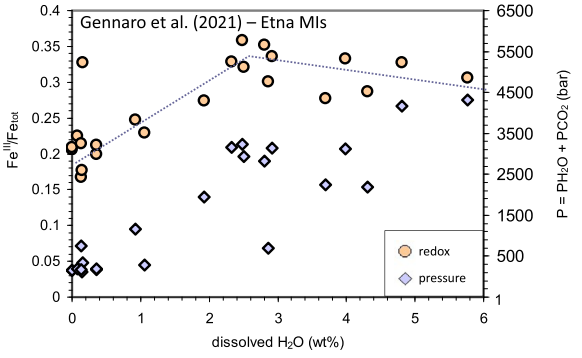

Figure 6. Dissolved H_2O versus Fe^{III}/Fe_{tot} ratios (circles; left *Y*-axis), measured by Fe-XANES [Gennaro et al., 2020; see Table 2]. Also reported are melt–fluid saturation pressures (diamond; right *Y*-axis) computed via the Papale et al. [2006].

Etna volcano. In particular, Figure 6 shows that in the Etnean magmas, (1) dehydration from ~6 wt% to ~2.5 wt% is associated with constant or even slightly increasing iron oxidation state, but (2) further dehydration is accompanied by iron reduction, with Fe^{III}/Fe_{tot} decreasing from about 0.32 to about 0.2.

Figure 6 plots also the total pressure (P = PH_2O + PCO_2) recalculated via Papale et al. [2006] with using for all MIs the average Etna composition of Table 1. We see that pressure decreases more or less regularly, but not following a unique decompression trend. This well-known behavior reflects the presence of different populations of melt inclusions equilibrated under different H_2O/CO_2 gas ratios and gas/melt proportion for the same pressure. These different populations are associated with different gas/melt proportions, mainly due to deep-gas fluxing: deeply exsolved and CO_2-dominated fluids rise through the plumbing system re-equilibrating with the magma at different depths and causing its dehydration [for a description of fluxing at Etna see also Métrich et al., 2004, Spilliaert et al., 2006, Aiuppa et al., 2007, Moretti et al., 2018]. This process also explains why at many open-conduit basaltic systems, including Etna, the onset of eruptions due to the arrival of deep and fresh magma is anticipated by periods of enhanced CO_2 degassing and by the increase in plume CO_2/S_{tot} ratios [Aiuppa et al., 2007, 2016, Paonita et al., 2021].

To understand more about the compositional role of water on fO_2 in a rising and degassing Etna basalt, we then consider the average Etna melt (Table 1), the Gennaro et al. [2020] water contents with pressures from the Papale et al. [2006] model (Figure 6) and attribute to all compositions the average Fe^{III}/Fe_{tot} ratio (0.27) from Gennaro et al. [2020] to calculate the fO_2 via the *IPA* and the *K&C* equation (Table 2).

We first perform computations by setting P ≈ PH_2O, that is, separating the sole effect of water, which affects melt polymerization, from that of CO_2, which in this system is the main fluid pressure medium. The results are plotted in Figure 7a,b and show that the *IPA* returns a range of ΔFMQ variations much narrower than that of the *K&C* equation, with an average ΔFMQ of 0.92. At very low H_2O contents, both models approach the ΔFMQ value from (36) (0.46). It is worth noting that the *K&C* equation transposes entirely the melt Fe^{III}/Fe_{tot} variations into fO_2 fluctuations (Figure 6). On the contrary, the *IPA* attributes a large part of the observed Fe^{III}/Fe_{tot} evolution to water content variations.

In terms of SO_2/H_2S gas ratios (Figure 7b; log-scale), both models calculate increasing ratios with increasing dehydration and thus decreasing PH_2O. This trend is however more marked and also well-defined for the *IPA* than the *K&C*. Compared to the Aiuppa et al. [2011] measured values (20–200; yellow semi-transparent box on the Y-axis), both models overestimate the SO_2/H_2S at PH_2O = 1 bar. However, we should remember that the observed range of values refer to passive (uneruptive) degassing, whereas magmas arriving at the surface are expected to carry larger SO_2/H_2S ratios. For the same reason, the passive degassing interval is very likely determined by magmas at PH_2O > 1 bar, up to almost 100 bar (Figure 7b).

By including PCO_2 (P_{tot} = PH_2O + PCO_2) (Figure 7c), computed ΔFMQ values for most hydrous datapoints are shifted to higher values compared to the previous case, particularly for the *IPA* results, whose average ΔFMQ is now 1.3. For dehydrated melts both models approach the ΔFMQ value (0.46) from (36). The *IPA* results follow a trend more similar to the *K&C* equation than previously, but this latter model still transfers almost completely to fO_2 the trend of Fe^{III}/Fe_{tot} variations observed in Figure 6. SO_2/H_2S gas ratios (log-scale) from both models are quite scattered when plotted versus P_{tot} (Fig-

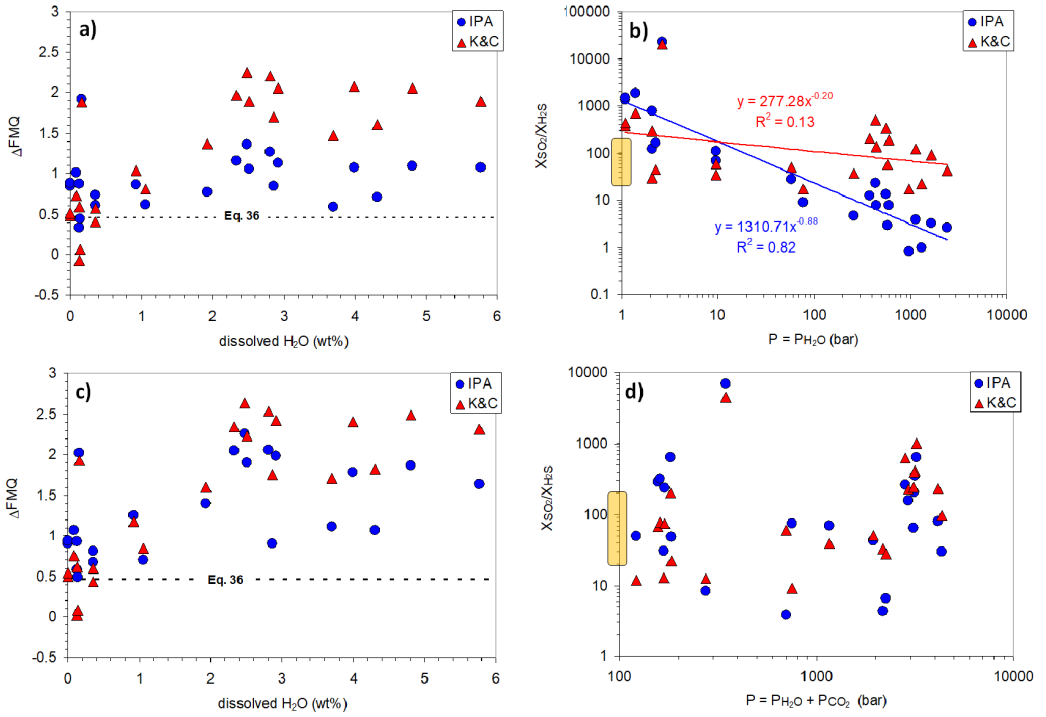

Figure 7. Results of the *IPA* and *K&C* computations of relative $\log fO_2$ (given as ΔFMQ; panels a,c) and SO_2/H_2S (panels b,d) for $P = PH_2O$ (panels a,b) and for $P_{tot} = PH_2O + PCO_2$ (panels c,d), as computed via Papale et al. [2006]. Also reported are the fO_2 value from (36) for Etna vents, extrapolated at 1150 °C (panels a,c) and the range of SO_2/H_2S variations (20–200) reported for Etna passive degassing (panels b,d).

ure 7d). Passive degassing values (20–200) are compatible with degassing magma at different depths.

In order to inspect how iron oxidation state varies for hydrous Etna compositions, I then run at 1150 °C the *K&C* model and the *IPA* based on the average Etna composition for the 42 H_2O–CO_2-saturated compositions reported in Moretti et al. [2018] (see Table 3). Missing the information on iron oxidation state in these samples, I compute the saturation pressures (Table 3) via Papale et al. [2006] by using the average Fe^{III}/Fe_{tot} ratio (0.27) from Gennaro et al. [2020] data (Table 2; Figure 6). Then, I calculate precisely the Fe^{III}/Fe_{tot} for these samples by imposing at all pressures the average fO_2 value corresponding to ΔFMQ = 1, which is intermediate to the averages returned by the *IPA* computations reported in Figure 7a,c.

Results of this exercise are given in Table 3 and Figure 8. The much larger reliability of the *IPA* in treating the role of composition, in this case due to water only, emerges from the trend sketched by modelled compositions. The *IPA* results at constant FMQ+1 adapt, at least in part, to the trend of Gennaro et al. [2020] data, telling us that a part of Fe^{III}/Fe_{tot} variations are due to the compositional variations determined by water content. Instead, the *K&C* model returns no variations of Fe^{III}/Fe_{tot} with the H_2O content (Figure 8). This is in line with the results in Figure 7a,c, which showed that the *K&C* equation in the range of conditions of interest here actually is insensitive to water content and turns all the fluctuations in Fe^{III}/Fe_{tot} into fO_2 variations.

Therefore, we can conclude that dehydration of Etna basalt at some point ($H_2O \approx 2.5$ wt%, from the data of Gennaro et al. [2020]) produces iron reduction, which takes place up to the surface also for a constant relative fO_2 corresponding to FMQ+1. Besides, the difference in slope of trends in Figure 8 is such that on the reduction due to dehydration part

Table 2. Iron oxidation state (by XANES) and dissolved H_2O and CO_2 content of Etna MIs from Gennaro et al. [2020]

Sample name	Fe^{III}/Fe_{tot}	H_2O (wt%)	CO_2 (ppm)	P_{tot} (bar)
FS-XS_8	0.306	5.77	2652	2387.3
FS-XS_15	0.274	1.93	900	259.6
FS-XS_20	0.352	2.81	1526	555.3
FS-XS_22a	0.327	4.81	2786	1650.6
FS-XS_22b	0.329	2.33	2033	380
FS-XS_26b	0.301	2.86	50	575.5
FS-XS_28a	0.358	2.48	2079	431.2
FS-XS_28b	0.336	2.92	1892	600.2
FS-XS_30	0.321	2.51	1106	441.8
FS-XS_35	0.333	3.99	1632	1130
FS-XS_41	0.287	4.31	687	1321
FS_00*	0.277	3.7	882	970
Spa_3n*	0.328	0.16	50	2.7
2002_26*	0.2	0.36	50	9.6
2002_30*	0.229	1.06	50	77.7
2002_32 matrix gl*	0.206	0	50	1.1
2006_4*	0.248	0.92	470	58.5
2006_7emb*	0.212	0.36	50	9.6
2008_1*	0.168	0.13	430	2.1
2008_6A*	0.209	0	50	1.1
2013_30*	0.177	0.14	50	2.3
2013_33*	0.225	0.08	50	1.4
2013_34*	0.214	0.13	50	2.1
Average	0.27			

Saturation pressure (P_{tot}) was computed from the model of Papale et al. [2006].

of the diagram (H_2O < 2.5 wt%) $A'B'_{slope} < AB_{slope}$, whereas on the oxidation due to dehydration side (H_2O > 2.5 wt%) $B'C'_{slope} > BC_{slope}$. This indicates that the *IPA* could match the trends of the Gennaro et al. [2020] XANES data by fine-tuning fO_2 to values higher than FMQ+1 with increasing pressure, hence depth. The Gennaro et al. [2020] data then point to fO_2 being higher at depth than at vent conditions, but the fO_2 decrease on magma rise is less or even much less significant than the one that can be computed via the *K&C* equation if this were used to fit the XANES data, as in the case of results in Figure 7c.

Finally, Figure 9 combines all available data to show that Etna MIs bear information on several degassing patterns with pressure (depth), resulting from the combination of two extremes processes: (1) decompression degassing, producing a gas phase enriched in H_2O on magma rise, and (2) CO_2-fluxing, leading to CO_2-dominated gas phase at shallow depths and also at vent conditions. Both mechanisms yield melt dehydration [Spilliaert et al., 2006, Blundy et al., 2010, Oppenheimer et al., 2011, Pino et al., 2011, Moretti et al., 2013a,b, 2018, 2019] and result in a generally positive correlation between melt Fe^{III}/Fe_{tot} and XH_2O in the exsolved gas phase. Nevertheless, negative correlations yielding trends of oxidation with dehydration at high water content (see trends BC and B′C′ in Figure 8) can be appreciated.

Table 3. Dissolved H_2O and CO_2 content of Etna MIs from Moretti et al. [2018], also including data from Del Carlo and Pompilio [2004]

H_2O (wt%)	CO_2 (ppm)	P (bar)	$X_{H_2O_{gas}}$ (mol)	Fe^{III}/Fe_{tot}		Source
				IPA	*K&C*	
2.22	272	952.0	0.369	0.282	0.243	Del Carlo and Pompilio [2004]
1.02	283	836.7	0.969	0.241	0.246	Del Carlo and Pompilio [2004]
2.25	503	1392.2	0.325	0.262	0.240	Del Carlo and Pompilio [2004]
2.86	880	2830.2	0.348	0.226	0.228	Del Carlo and Pompilio [2004]
3.13	576	1677.1	0.456	0.275	0.236	Del Carlo and Pompilio [2004]
1.26	289	876.5	0.204	0.249	0.246	Del Carlo and Pompilio [2004]
1.56	451	1201.7	0.214	0.247	0.243	Del Carlo and Pompilio [2004]
2.63	266	1862.4	0.502	0.253	0.236	Del Carlo and Pompilio [2004]
3.04	207	1847.7	0.624	0.265	0.235	Del Carlo and Pompilio [2004]
2.55	615	1614.4	0.348	0.262	0.238	Del Carlo and Pompilio [2004]
1.94	221	841.2	0.390	0.277	0.245	Del Carlo and Pompilio [2004]
1.94	1404	2561.4	0.235	0.214	0.231	Del Carlo and Pompilio [2004]
1.94	3	292.0	0.967	0.307	0.249	Del Carlo and Pompilio [2004]
1.94	210	803.6	0.378	0.279	0.245	Del Carlo and Pompilio [2004]
1.94	0	220.0	0.998	0.311	0.250	Del Carlo and Pompilio [2004]
1.29	811	1693.7	0.126	0.221	0.239	Moretti et al. [2018]
1.29	539	1306.3	0.153	0.234	0.242	Moretti et al. [2018]
1.39	474	1216.5	0.180	0.240	0.243	Moretti et al. [2018]
1.25	720	1565.4	0.128	0.224	0.240	Moretti et al. [2018]
2.10	323	1864.1	0.362	0.239	0.236	Moretti et al. [2018]
0.95	415	1865.5	0.118	0.206	0.239	Moretti et al. [2018]
0.54	226	675.3	0.083	0.228	0.249	Moretti et al. [2018]
3.02	708	1837.7	0.405	0.265	0.235	Moretti et al. [2018]
1.60	149	631.3	0.375	0.274	0.247	Moretti et al. [2018]
1.60	149	631.3	0.375	0.274	0.247	Moretti et al. [2018]
1.99	200	886.6	0.418	0.277	0.244	Moretti et al. [2018]
1.99	200	886.6	0.418	0.277	0.244	Moretti et al. [2018]
1.31	81	421.0	0.402	0.272	0.249	Moretti et al. [2018]
1.31	81	421.0	0.402	0.272	0.249	Moretti et al. [2018]
1.31	81	421.0	0.402	0.272	0.249	Moretti et al. [2018]
1.31	81	421.0	0.402	0.272	0.249	Moretti et al. [2018]
2.50	140	782.0	0.596	0.301	0.244	Moretti et al. [2018]
2.50	140	782.0	0.596	0.301	0.244	Moretti et al. [2018]
1.88	92	540.7	0.540	0.290	0.247	Moretti et al. [2018]
1.88	92	540.7	0.540	0.290	0.247	Moretti et al. [2018]
2.08	546	1430.2	0.284	0.255	0.240	Moretti et al. [2018]
2.08	546	1430.2	0.284	0.255	0.240	Moretti et al. [2018]

(continued on next page)

Table 3. (continued)

H_2O (wt%)	CO_2 (ppm)	P (bar)	$X_{H_2O_{gas}}$ (mol)	Fe^{III}/Fe_{tot}		Source
				IPA	*K&C*	
3.24	1833	3118.8	0.307	0.225	0.225	Moretti et al. [2018]
3.24	1833	3118.8	0.307	0.225	0.225	Moretti et al. [2018]
2.86	717	1817.2	0.377	0.261	0.235	Moretti et al. [2018]
2.86	717	1817.2	0.377	0.261	0.235	Moretti et al. [2018]
1.74	532	1356.5	0.228	0.247	0.241	Moretti et al. [2018]
1.74	532	1356.5	0.228	0.247	0.241	Moretti et al. [2018]
1.76	532	1356.5	0.228	0.248	0.241	Moretti et al. [2018]
1.75	532	1356.5	0.228	0.247	0.241	Moretti et al. [2018]
2.50	94	674.8	0.673	0.307	0.245	Moretti et al. [2018]
3.50	1136	2464.2	0.405	0.250	0.230	Moretti et al. [2018]

Saturation pressure (P_{tot}) and gas phase composition were computed from the model of Papale et al. [2006]. Also reported are the iron oxidation ratios calculated via the *K&C* (6) and the *IPA* (summarized by model (19)) at FMQ+1.

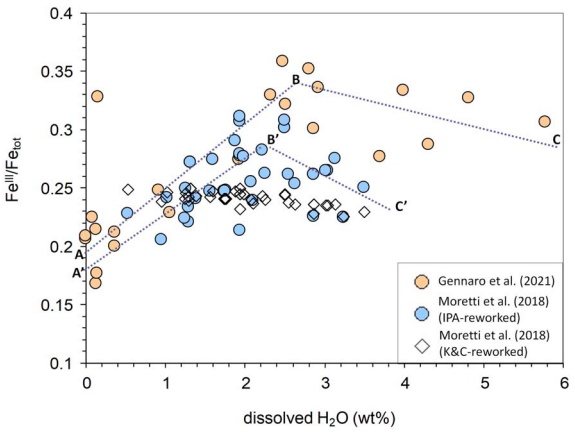

Figure 8. Dissolved H_2O versus Fe^{III}/Fe_{tot} ratios measured via XANES by Gennaro et al. [2020] (see Table 2) and from MIS reported in Moretti et al. [2018] (Table 3) computed at FMQ+1 via the *IPA* and the *K&C* equation. Note that secondary phenomena (post entrapment crystallization and H^+ diffusion) may have affected measured MI oxidation states, yielding iron oxidation. Although these were approximately evaluated by Gennaro et al. [2020] to shift positively the Fe^{III}/Fe_{tot} ratio of at most 0.06 units for most hydrated samples, they cannot be precisely assessed and then ruled out.

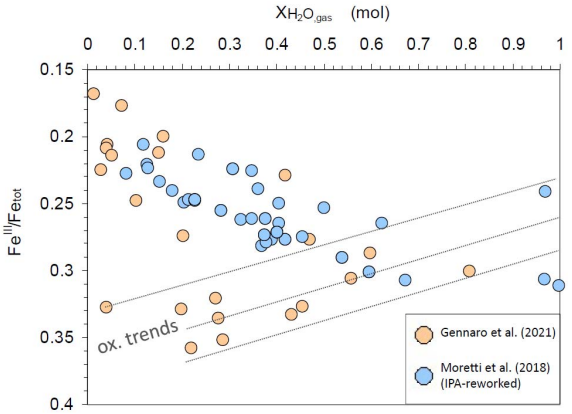

Figure 9. Molar water proportion in the exsolved gas ($X_{H_2O_{gas}}$) versus measured or computed Fe^{III}/Fe_{tot} ratios for MIs from Gennaro et al. [2020; measured Fe^{III}/Fe_{tot} ratios via XANES; see Table 2] and from Moretti et al. [2018] (Table 3, IPA-computed Fe^{III}/Fe_{tot} ratios at FMQ+1). Redox variations occur in the 0.1 MPa–432 MPa range of total pressure [via the Papale et al. [2006] fluid–melt saturation model].

5. Discussion and conclusions

The characterization of melt inclusions in terms of dissolved volatiles and oxidation state of iron and sulfur has allowed a vast amount of assessments of volcano-magmatic fluid speciation and evolution from depth to surface vents, where discharged gases are measured. A critical issue is represented by the magma redox evolution, which is typically reported as the oxygen fugacity, fO_2. Tracking redox evolution and fluid speciation via modelling of melt–fluid saturation plus fO_2 in different environments from the magma source at depth to the surface is challenging, even at equilibrium conditions and for well-established relations about solid–liquid–gas exchanges. The use of empirical expression may do the required job, but without a clear appraisal of the reactive nature of silicate melts, any redox assessment can be biased. Oxygen fugacity, in particular, is a parameter that cannot be treated as a Maxwell's demon or an adjustable parameter to fit the experimental data. Determination of fO_2 from melts/glasses demands accounting for the role of bulk composition, which shifts the redox properties through the reactive behavior of the silicate network, that is, its polymerization.

Therefore, the right choice of models is strategic for (1) the petrologic interpretation of plumbing systems, (2) the definition of magma processes throughout the P–T conditions encountered during magma differentiation and rise, and (3) the prompt evaluation of the magma state based on the monitoring of volcanic gases.

In many studies [e.g. Oppenheimer et al., 2011, Moussallam et al., 2014, 2016, 2019], it is shown that fO_2 tends to decrease on magma rise and decompression degassing [path P2 in Figure 1; see also Moretti and Stefansson, 2020], at least if the melt contains iron [Burgisser and Scaillet, 2007]. However, the fact that the fO_2 signature of deep magmas is lost because fO_2 decreases on magma rise sounded counterintuitive to many. However, if we simply consider the Total Oxygen/Total Cations ratio from melt formulas, we see that an olivine melt has a value of 4/3, orthopyroxene and clinopyroxene 3/2, whereas silica has a value of 2 and albite of 8/5. By including water, the Total Oxygen/Total Cations ratio tends to increase even more with the progressive dehydration taking place on decompression. So, we should expect fO_2 increasing toward the surface simply because magmatic differentiation, which includes degassing and dehydration, points to increasing the relative amount of oxygen in the melt. However, magma rise and differentiation imply increasing polymerization, particularly via melt dehydration, which decreases the amount of reactive oxygen, measured by $[O^{2-}]$. Because O^{2-} activity is directly related to fO_2 via the oxygen electrode (reaction (13)) we can then easily figure out why, at a given temperature, fO_2 decreases. This behavior is then a reflex of the fact that in silicate melts, oxygen *tout court* cannot be identified as the solvent, despite its nominal abundance [Allanore, 2015, Moretti, 2021, Moretti and Ottonello, 2022]. Nevertheless, fO_2 decrease does not mean necessarily iron reduction: this is seen in Figure 4b, for the same Fe^{III}/Fe_{tot} values of both shallow and deep Etna basalt, and in Figure 9, where a change of trivalent iron speciation clearly intervenes at $H_2O \approx 2.5$ wt%. Therefore, speciation state, which in melts depends on composition and polymerization, is a one of the major controls of the oxidation state of multivalent elements dissolved in melts. In particular, at large depths the fO_2 decrease upon magma differentiation does not correspond necessarily to iron reduction (Figure 9).

In this study we have shown the performances of different oxybarometers at 1 bar and also at pressures corresponding to H_2O–CO_2-melt saturation. The following recommendations and main points emerge:

(1) because the assessment of volatile amounts is central, MIs' representativeness must be fully understood. This demands a large set of MIs for statistical treatment [e.g., Barsanti et al., 2009] as well as Raman characterization of shrinkage bubbles to quantify CO_2 loss to the bubble [Venugopal et al., 2020, and references therein]. Recommended practices to follow can be found in Rose-Koga et al. [2021].

(2) The Etna example of this study, based on the Fe-XANES data of Gennaro et al. [2020], shows that empirical iron-oxybarometers, such as the *K&C* equation (6), compute fO_2 decrease, but because magma evolution is about oxygen-based reactions, reactive-species models accounting for melt nature, particularly polymerization, can provide more precise estimates of these variations. In particular, in the case of Etna, the fO_2 decrease on melt rise is less important when assessed via the *IPA* than via the *K&C* equation. This is because of the role played by wa-

ter in modulating redox transfers via the melt network and the activity of O^{2-}, $[O^{2-}]$, hence the oxygen electrode. In the specific case of Etna, at FMQ+1 the *IPA* predicts iron reduction on dehydration for $H_2O < 2$ wt%, but oxidation, or no change within approximation, for dehydration occurring at $H_2O > 2$ wt% (Figure 8). We see that even at constant relative fO_2, depending on composition (the water content) dehydration-induced decrease of $[O^{2-}]$ may either favour Fe^{2+} via reaction (9) or Fe^{3+} via reaction (7). Interestingly, the experimental Gennaro et al. [2020] data show clearly the threshold between these two mechanisms for H_2O-contents around 2.5 wt%. This behavior, which recalls very closely that shown by the Dickenson and Hess [1982] data for increasing K_2O in SiO_2–Al_2O_3–Fe_2O_3–FeO–K_2O systems equilibrated on air [see also Cicconi et al., 2020a, Moretti, 2021, Moretti and Ottonello, 2022], is then partially captured by the *IPA* at constant FMQ+1. Interestingly, this behavior might imply that for $P \approx 3$ kbar (the pressure corresponding to the oxidation–reduction threshold in Figure 6) Etna melts record the change of speciation of trivalent iron reported at around 4 kbar by Moretti and Ottonello [2022] on the basis of completely independent volume-compressibility arguments on volatile-free melts.

(3) For both basalt and andesite, the 1-bar *IPA* model is definitely the one returning most of the sulfur oxidation at a given Fe^{III}/Fe_{tot}, hence fO_2, condition (Figure 3). However, the IPA model is expected to be the one more precisely calibrated at 1 bar, because its accuracy results from the accuracies in reproducing a vast domain of 1-bar solubility data and sulfide–sulfate capacities (reactions (20), (21) and (22)–(27)). On the other hand, all the other models (*Ju*, *NSW*, *W&C*) do not consider the role of pressure, but were calibrated on sulfur oxidation/speciation data from samples quenched from high pressure equilibrium experiments. Therefore, these formulations are not intended to work at 1 bar. This argument can be appreciated if we consider that the *Ju* and *W&C* models cannot reproduce the 1-bar S-oxidation state in the SiO_2–Na_2O join at 1250 °C by Nagashima and Katsura [1973], whereas the *IPA* model does [Moretti and Ottonello, 2005, Moretti, 2021, Papale et al., 2022] by accounting for compositional effects, which are exacerbated in a simple silica–alkali binary system [Allanore, 2015, Moretti and Neuville, 2021, Moretti and Ottonello, 2022]. Basically, the *IPA* and *NSW* models ((27) and (33), respectively) show largest variations of S^{6+}/S_{tot}, but for two different reasons: composition for the *IPA*, temperature for the *NSW*. On the other side the *W&C* and *Ju* equations (30) and (31) are the most "static" models to report S^{6+}/S_{tot} versus another redox indicator such as fO_2 or Fe^{III}/Fe_{tot}: if at a given temperature they each show slight variations from one composition to another, like andesite to basalt in Figure 3f, this is simply because composition plays some role in shifting the fO_2 calculated from Fe^{III}/Fe_{tot} via the *K&C* equation (6).

(4) For H_2O–CO_2-saturated melts, the pressure and X_{CO_2} behaviors shown in Figures 4a and particularly 4b testify for the strong non-linearities due to composition, especially at high pressure and in the presence of significant amounts of iron, such as in basalts. Whether these non-linearities are in part due to model uncertainties or to the physics of dissolution, it is clear that any model can be improved by implementing the calibration database wherever counterintuitive features are observed.

The exsolution of the gas/fluid mixture is a form of magmatic differentiation that depends on the melt–volatile saturation state (or "volatile mixed-solubility" in some literature), which is related to speciation and hence fO_2. Again, the composition of the whole system is the key and at equilibrium it is futile to discriminate "what controls what". Certainly, the interplay of compositional variables, plus pressure and temperature regimes, makes every volcano unique.

(5) Oxygen, or at least a part of it, should be considered as a fluid mobile component, basically meaning that from depth to surface its amount in the system is not fully pre-determined but may slightly vary: in volcanic degassing studies we tend in fact to picture the magma as essentially a two-phase melt–fluid system. Magma is however a multiphase system that includes many solid solutions (the minerals) and in which all phases dissolve oxygen or are dominated by it. In this context, the two mobile phases, fluid and melt, are highly reactive and exchange with the surrounding rocks and fluids, from mantle though crust, up to the surface. Although the big capacitors of mobile oxygen are FeO and Fe_2O_3 components, particularly in basalt, in such a scenario pre-determining the amount of oxygen like in some forward models [e.g. Burgisser and Scaillet, 2007] may unrealistically constrain fO_2, a *de facto* virtual parameter (be-

cause it is about an undetectable species) but with a strong thermodynamic meaning [Ghiorso and Kelemen, 1987, Cicconi et al., 2020b, Moretti and Stefansson, 2020, Moretti and Neuville, 2021]. For these reasons, Moretti and Papale [2004] avoid the oxygen mass balance.

Even though iron is the most used reference element to express the reducing or oxidized conditions of the different envelopes, it is important to remember that magmas are enriched also in other minor multivalent elements, such as Cr, V, Ce, Eu etc. [e.g., Berry et al., 2006, Mallmann et al., 2021, and references therein; Cicconi et al., 2021, and references therein]. In geological melts, these elements are only present at low abundances relative to Fe, so their redox exchange minimally affects the Fe^{III}/Fe_{tot} ratio. However, redox equilibria of these elements are all potential oxybarometers and their characterization and translation of their oxidation state into fO_2 [e.g., Fraser, 1975, Berry and O'Neill, 2004, Karner et al., 2007, Mallmann et al., 2021] can be fundamental to solve melt–fluid speciation issues.

Code availability

The iron-redox code [Ottonello et al., 2001, Moretti, 2005] can be accessed from https://github.com/charlesll/iron-magma.

The CTFSFG code [Moretti and Ottonello, 2005] can be accessed from https://github.com/charlesll/sulfur-magma.

At these sites, Fortran source codes are available together with instructions to run them and relevant information on licensing and credit to be given.

Conflicts of interest

The author has no conflict of interest to declare.

Acknowledgements

I wish to thank the volume editor, Dr. D. R. Neuville, and two anonymous reviewers who helped improving the quality of the manuscript. This study contributes to the IdEx Université de Paris ANR-18-IDEX-0001.

References

Aiuppa, A., Allard, P., Bernard, B., Lo Forte, F. M., Moretti, R., and Hidalgo, S. (2022). Gas leakage from shallow ponding magma and trapdoor faulting at Sierra Negra volcano (Isabela Island, Galápagos). *Geochem. Geophys. Geosyst.*, 23, article no. e2021GC010288.

Aiuppa, A., Bertagnini, A., Métrich, N., Moretti, R., Di Muro, A., Liuzzo, M., and Tamburello, G. (2010). A degassing model for Stromboli volcano. *Earth Planet. Sci. Lett.*, 295(2010), 195–204.

Aiuppa, A., Bitetto, M., Francofonte, V., Velasquez, G., Bucarey Parra, C., Giudice, G., Liuzzo, M., Moretti, R., Moussallam, Y., Peters, N., Tamburello, G., Valderrama, A., and Curtis, A. (2017). A CO_2-gas precursor to the March 2015 Villarrica volcano eruption. *Geochem. Geophys. Geosyst.*, 18(6), 2120–2132.

Aiuppa, A., de Moor, J. M., Arellano, S., Coppola, D., Francofonte, V., Galle, B., Giudice, G., Liuzzo, M., Mendoza, E., Saballos, A., Tamburello, G., Battaglia, A., Bitetto, M., Gurrieri, S., Laiolo, M., Mastrolia, A., and Moretti, R. (2018). Tracking formation of a lava lake from ground and space: Masaya Volcano (Nicaragua). *Geochem. Geophys. Geosyst.*, 19(2), 496–515.

Aiuppa, A., Federico, C., Giudice, G., Giuffrida, G., Guida, R., Guerrieri, S., Liuzzo, M., Moretti, R., and Papale, P. (2009). The 2007 eruption of Stromboli volcano: insights from real-time measurement of the volcanic gas plume CO_2/SO_2 ratio. *J. Volcanol. Geotherm. Res.*, 189, 221–230.

Aiuppa, A., Lo Coco, E., Liuzzo, M., Giudice, G., Giuffrida, G., and Moretti, R. (2016). Terminal Strombolian activity at Etna's central craters during summer 2012: the most CO_2-rich volcanic gas ever recorded at Mount Etna. *Geochem. J.*, 50, 123–138.

Aiuppa, A., Moretti, R., Federico, C., Giudice, G., Guerrieri, S., Liuzzo, M., Papale, P., Shinohara, H., and Valenza, M. (2007). Forecasting Etna eruptions by real-time observation of volcanic gas composition. *Geology*, 35, 1115–1118.

Aiuppa, A., Shinohara, H., Tamburello, G., Giudice, G., Liuzzo, M., and Moretti, R. (2011). Hydrogen in the gas plume of an open-vent volcano (Mt. Etna, Italy). *J. Geophys. Res.*, 116, article no. B10204.

Aiuppa, A., Tamburello, G., Di Napoli, R., Cardellini, C., Chiodini, G., Giudice, G., Frassa, F., and Pedone,

M. (2013). First observations of the fumarolic gas output from a restless caldera: implications for the current period of unrest (2005–2013) at Campi Flegrei. *Geochem. Geophys. Geosyst.*, 14(10), 4153–4169.

Allanore, A. (2013). Electrochemical engineering of anodic oxygen evolution in molten oxides. *Electrochim. Acta*, 110, 587–592.

Allanore, A. (2015). Features and challenges of molten oxide electrolytes for metal extraction. *J. Electrochem. Soc.*, 162, E13–E22.

Allard, P. (2010). A CO_2-rich gas trigger of explosive paroxysms at Stromboli basaltic volcano, Italy. *J. Volcanol. Geotherm. Res.*, 189(3–4), 363–374.

Allard, P., Aiuppa, A., Bani, P., Métrich, N., Bertagnini, A., Gauthier, P. J., Shinohara, H., Sawyer, G., Parello, F., Bagnato, E., Pelletier, B., and Garaebiti, E. (2016). Prodigious emission rates and magma degassing budget of major, trace and radioactive volatile species from Ambrym basaltic volcano, Vanuatu island Arc. *J. Volcanol. Geotherm. Res.*, 322, 119–143.

Allison, C. M., Roggensack, K., and Clarke, A. B. (2021). Highly explosive basaltic eruptions driven by CO_2 exsolution. *Nat. Commun.*, 12(1), 1–10.

Arienzo, I., Mazzeo, F. C., Moretti, R., Cavallo, A., and D'Antonio, M. (2016). Open-system magma evolution and fluid transfer at Campi Flegrei caldera (Southern Italy) during the past 5 ka as revealed by geochemical and isotopic data: the example of the Nisida eruption. *Chem. Geol.*, 427(2016), 109–124.

Arienzo, I., Moretti, R., Civetta, L., Orsi, L., and Papale, P. (2010). The feeding system of the Agnano-Monte Spina eruption (Campi Flegrei, Italy): dragging the past into present activity and future scenarios. *Chem. Geol.*, 270, 135–147.

Baker, D. R. and Moretti, R. (2011). Modeling the solubility of sulfur in magmas: a 50-year old geochemical challenge. *Rev. Mineral Geochem.*, 73, 167–213.

Barsanti, M., Papale, P., Barbato, D., Moretti, R., Hauri, E., Boschi, E., and Longo, A. (2009). Heterogeneous large total CO_2 abundance in the shallow magmatic system of Kilauea volcano, Hawaii. *J. Geophys. Res.*, 114, article no. B12201.

Behrens, H. and Gaillard, F. (2006). Geochemical aspects of melts: volatiles and redox behavior. *Elements*, 2(5), 275–280.

Berry, A. J. and O'Neill, H. S. C. (2004). A XANES determination of the oxidation state of chromium in silicate glasses. *Am. Mineral.*, 89(5–6), 790–798.

Berry, A. J., O'Neill, H. S. C., Scott, D. R., Foran, G. J., and Shelley, J. M. G. (2006). The effect of composition on Cr^{2+}/Cr^{3+} in silicate melts. *Am. Mineral.*, 91, 1901–1908.

Blundy, J., Cashman, K. V., Rust, A., and Witham, F. (2010). A case for CO_2-rich arc magmas. *Earth Planet. Sci. Lett.*, 290(3–4), 289–301.

Boichu, M., Villemant, B., and Boudon, G. (2008). A model for episodic degassing of an andesitic magma intrusion. *J. Geophys. Res.*, 113, article no. B07202.

Boichu, M., Villemant, B., and Boudon, G. (2011). Degassing at La Soufrière de Guadeloupe volcano (Lesser Antilles) since the last eruptive crisis in 1975–77: result of a shallow magma intrusion? *J. Volcanol. Geotherm. Res.*, 203(3–4), 102–112.

Borisov, A., Behrens, H., and Holtz, F. (2018). Ferric/ferrous ratio in silicate melts: a new model for 1 atm data with special emphasis on the effects of melt composition. *Contrib. Mineral Petrol*, 173, 1–15.

Brounce, M., Stolper, E., and Eiler, J. (2017). Redox variations in Mauna Kea lavas, the oxygen fugacity of the Hawaiian plume, and the role of volcanic gases in Earth's oxygenation. *Proc. Natl. Acad. Sci. USA*, 114(34), 8997–9002.

Buddington, A. F. and Lindsley, D. H. (1964). Iron–titanium oxide minerals and synthetic equivalents. *J. Petrol.*, 5, 310–357.

Burgisser, A. and Scaillet, B. (2007). Redox evolution of a degassing magma rising to the surface. *Nature*, 445(7124), 194–197.

Caliro, S., Chiodini, G., Moretti, R., Avino, R., Granieri, D., Russo, M., and Fiebig, J. (2007). The origin of the fumaroles of La Solfatara (Campi Flegrei, south Italy). *Geochim. Cosmochim. Acta*, 71(12), 3040–3055.

Caricchi, L., Sheldrake, T. E., and Blundy, J. (2018). Modulation of magmatic processes by CO_2 flushing. *Earth Planet. Sci. Lett.*, 491, 160–171.

Carmichael, I. S. E. (1966). The iron–titanium oxides of salic volcanic rocks and their associated ferromagnesian silicates. *Contrib. Mineral. Petrol.*, 14, 36–64.

Carmichael, I. S. E. and Nicholls, J. (1967). Iron–titanium oxides and oxygen fugacities in volcanic rocks. *J. Geophys. Res.*, 72, 4665–4687.

Carroll, M. R. and Rutherford, M. J. (1988). Sulfur

speciation in hydrous experimental glasses of varying oxidation state: results from measured wavelength shifts of sulfur X-rays. *Am. Mineral.*, 73, 845–849.

Carroll, M. R. and Webster, J. D. (1994). Solubilities of sulfur, noble gases, nitrogen, chlorine, and fluorine in magmas. *Rev. Mineral. Geochem.*, 30, 231–279.

Cicconi, M. R., Le Losq, C., Henderson, G., and Neuville, D. R. (2021). The redox behavior of rare earth elements. In Moretti, R. and Neuville, D. R., editors, *Magma Redox Geochemistry*, volume 266 of *Geophysical Monograph, American Geophysical Union*, pages 381–398. John Wiley & Sons, Inc., Hoboken, NJ, USA.

Cicconi, M. R., Le Losq, C., Moretti, R., and Neuville, D. R. (2020a). Magmas are the largest repositories and carriers of earth's redox processes. *Elements*, 16, 173–178.

Cicconi, M. R., Moretti, R., and Neuville, D. R. (2020b). Earth's electrodes. *Elements*, 16, 157–160.

D'Antonio, M., Tonarini, S., Arienzo, I., Civetta, L., Dallai, L., Moretti, R., Orsi, G., Andria, M., and Trecalli, A. (2013). Discerning mantle and crustal processes within the Roman Province: insights from mineralogy, geochemistry, and Sr–Nd–O isotopes of young hybrid volcanics from the Ischia island (South Italy). *Contrib. Mineral. Petrol.*, 165, 1173–1194.

Del Carlo, P. and Pompilio, M. (2004). The relationship between volatile content and the eruptive style of basaltic magma: the Etna case. *Ann. Geophys.*, 47, 1423–1432.

Dickenson, M. P. and Hess, P. C. (1982). Redox equilibria and the structural role of iron in aluminosilicate melts. *Contrib. Mineral Petrol.*, 78, 352–357.

Duffy, J. A. (1993). A review of optical basicity and its applications to oxidic systems. *Geochim. Cosmochim. Acta*, 57, 3961–3970.

Edmonds, M., Aiuppa, A., Humphreys, M., Moretti, R., Giudice, G., Martin, R., Herd, R. A., and Christopher, T. (2010). Excess volatiles supplied by mingling of mafic magma at an andesitic arc volcano. *Geophys. Geochem. Geosyst.*, 11(4), article no. Q04005.

Edmonds, M. and Wallace, P. J. (2017). Volatiles and exsolved vapor in volcanic systems. *Elements*, 13(1), 29–34.

Esposito, R., Bodnar, R. J., Danyushevsky, L. V., De Vivo, B., Fedele, L., Hunter, J., Lima, A., and Shimizu, N. (2011). Volatile evolution of magma associated with the Solchiaro eruption in the Phlegrean Volcanic District (Italy). *J. Petrol.*, 52(12), 2431–2460.

Fincham, C. J. B. and Richardson, F. D. (1954). The behaviour of sulphur in silicate and aluminate melts. *Phil. Trans. R. Soc. Lond. Ser. A*, 223, 40–62.

Floris, F. M. and Tomasi, J. (1989). Evaluation of the dispersion contribution to the solvation energy. A simple computational model in the continuum approximation. *J. Comput. Chem.*, 10, 616–627.

Floris, F. M., Tomasi, J., and Pascual-Ahuir, J. L. (1991). Dispersion and repulsion contributions to the solvation energy: refinements to a simple computational model in the continuum approximation. *J. Comput. Chem.*, 12, 784–791.

Fraser, D. G. (1975). Activities of trace elements in silicate melts. *Geochim. Cosmochim. Acta*, 39, 1525–1530.

Frost, B. R. (1991). Introduction to oxygen fugacity and its petrologic importance. *Rev. Mineral. Geochem.*, 25, 1–9.

Gaborieau, M., Laubier, M., Bolfan-Casanova, N., McCammon, C. A., Vantelon, D., Chumakov, A. I., Schiavi, F., Neuville, D. R., and Venugopal, S. (2020). Determination of $Fe^{3+}/\Sigma Fe$ of olivine-hosted melt inclusions using Mössbauer and XANES spectroscopy. *Chem. Geol.*, 547, article no. 119646.

Gennaro, E., Paonita, A., Iacono-Marziano, G., Moussallam, Y., Pichavant, M., Peters, N., and Martel, C. (2020). Sulphur behaviour and redox conditions in etnean magmas during magma differentiation and degassing. *J. Petrol.*, 61(10), article no. egaa095.

Ghiorso, M. S. and Kelemen, P. B. (1987). Evaluating reaction stoichiometry in magmatic systems evolving under generalized thermodynamic constraints: examples comparing isothermal and isenthalpic assimilation. *Magmatic Process.: Physicochem. Principles*, 1, 319–336.

Giggenbach, W. F. (1987). Redox processes governing the chemistry of fumarolic gas discharges from White Island, New Zealand. *Appl. Geochem.*, 2, 143–161.

Gurenko, A. A., Trumbull, R. B., Thomas, R., and Lindsay, J. M. (2005). A melt inclusion record of volatiles, trace elements and Li–B isotope variations in a single magma system from the Plat Pays Volcanic Complex, Dominica, Lesser Antilles. *J. Petrol.*, 46(12), 2495–2526.

Hartley, M. E., Maclennan, J., Edmonds, M., and Thordarson, T. (2014). Reconstructing the deep CO_2 degassing behaviour of large basaltic fissure eruptions. *Earth Planet. Sci. Lett.*, 393, 120–131.

Hartley, M. E., Shorttle, O., Maclennan, J., Moussallam, Y., and Edmonds, M. (2017). Olivine-hosted melt inclusions as an archive of redox heterogeneity in magmatic systems. *Earth Planet. Sci. Lett.*, 479, 192–205.

Hauri, E. (2002). SIMS analysis of volatiles in silicate glasses, 2: isotopes and abundances in Hawaiian melt inclusions. *Chem. Geol.*, 183(1–4), 115–141.

Hauri, E., Wang, J., Dixon, J. E., King, P. L., Mandeville, C., and Newman, S. (2002). SIMS analysis of volatiles in silicate glasses: 1. Calibration, matrix effects and comparisons with FTIR. *Chem. Geol.*, 183(1–4), 99–114.

Hedenquist, J. W. and Lowenstern, J. B. (1994). The role of magmas in the formation of hydrothermal ore deposits. *Nature*, 370(6490), 519–527.

Ihinger, P. D., Hervig, R. L., and McMillan, P. F. (1994). Analytical methods for volatiles in glasses. *Rev. Mineral.*, 30, 67–121.

Jayasuriya, K. D., O'Neill, H. S. C., Berry, A. J., and Campbell, S. J. (2004). A Mossbauer study of the oxidation state of Fe in silicate melts. *Am. Mineral.*, 89, 1597–1609.

Jugo, P. J. and Luth, R. W. (2005). Experimental data on the speciation of sulfur as a function of oxygen fugacity in basaltic melts. *Geochim. Cosmochim. Acta*, 69, 497–503.

Jugo, P. J., Wilke, M., and Botcharnikov, R. E. (2010). Sulfur K-edge XANES analysis of natural and synthetic basaltic glasses: implications for S speciation and S content as function of oxygen fugacity. *Geochim. Cosmochim. Acta*, 74, 5926–5938.

Karner, J. M., Papike, J. J., Shearer, C. K., McKay, G., Le, L., and Burger, P. (2007). Valence state partitioning of Cr and V between pyroxene-melt: estimates of oxygen fugacity for martian basalt QUE 94201. *Am. Mineral.*, 92(7), 1238–1241.

Klimm, K., Kohn, S. C., and Botcharnikov, R. E. (2012). The dissolution mechanism of sulphur in hydrous silicate melts. II: solubility and speciation of sulphur in hydrous silicate melts as a function of fO_2. *Chem. Geol.*, 322, 250–267.

Kress, V. C. and Carmichael, I. S. E. (1991). The compressibility of silicate liquids containing Fe_2O_3 and the effect of composition, temperature, oxygen fugacity and pressure on their redox states. *Contrib. Mineral Petrol.*, 108, 82–92.

Le Losq, C., Berry, A. J., Kendrick, M. A., Neuville, D. R., and O'Neill, H. S. C. (2019). Determination of the oxidation state of iron in mid-ocean ridge basalt glasses by Raman spectroscopy. *Am. Mineral.*, 104, 1032–1042.

Le Losq, C., Moretti, R., and Neuville, D. R. (2013). On the speciation and amphoteric behavior of water in aluminosilicate melts and glasses: high-temperature Raman spectroscopy and reaction equilibria. *Eur. J. Mineral.*, 25, 777–790.

Le Losq, C., Moretti, R., Oppenheimer, C., Baudelet, F., and Neuville, D. R. (2020). Dynamic *in situ* experimental Fe K-edge XANES study of iron oxidation state and coordination in magmas: application to Erebus phonolite. *Contrib. Mineral Petrol.*, 175, 1–13.

Le Losq, C., Neuville, D., Moretti, R., and Roux, J. (2012). Determination of water content in silicate glasses using Raman Spectrometry, with application to explosive volcanism. *Am. Mineral.*, 97, 779–790.

Le Losq, C., Neuville, D. R., Moretti, R., Kyle, P. R., and Oppenheimer, C. (2015). Rheology of phonolitic magmas—the case of the Erebus lava lake. *Earth Planet. Sci. Lett.*, 411, 53–61.

Lerner, A. H., Muth, M. J., Wallace, P. J., Lanzirotti, A., Newville, M., Gaetani, G. A., Chowdhury, P., and Dasgupta, R. (2021). Improving the reliability of Fe- and S-XANES measurements in silicate glasses: correcting beam damage and identifying Fe-oxide nanolites in hydrous and anhydrous melt inclusions. *Chem. Geol.*, 586, article no. 120610.

Lewis, G. N. and Randall, M. (1961). *Thermodynamics*. McGraw-Hill Book Company, New York, 2nd edition. (Revised by K. Pitzer, L. Brewer).

Mallmann, G., Burnham, A. D., and Fonseca, R. O. (2021). Mineral-melt partitioning of redox-sensitive elements. In Moretti, R. and Neuville, D. R., editors, *Magma Redox Geochemistry*, volume 266 of *Geophysical Monograph, American Geophysical Union*, pages 345–367. John Wiley & Sons, Inc., Hoboken, NJ, USA.

Mangiacapra, A., Moretti, R., Rutherford, M., Civetta, L., Orsi, G., and Papale, P. (2008). The deep magmatic system of the Campi Flegrei caldera (Italy). *Geophys. Res. Lett.*, 35, article no. L21304.

Manzini, M., Bouvier, A. S., Barnes, J. D., Bonifacie,

M., Rose-Koga, E. F., Ulmer, P., Métrich, N., Bardoux, G., Williams, J., Layne, G., Straub, S., Lukas, P., Baumgartner, L., and John, T. (2017). SIMS chlorine isotope analyses in melt inclusions from arc settings. *Chem. Geol.*, 449, 112–122.

Matthews, S. J., Moncrieff, D. H. S., and Carroll, M. R. (1999). Empirical calibration of the sulphur valence oxygen barometer from natural and experimental glasses: method and applications. *Mineral Mag.*, 63, 421–431.

Maurel, C. and Maurel, P. (1982). Étude expérimentale de la distribution de l'aluminium entre bain silicaté basique et spinelle chromifère. Implications pétrogénétiques : teneur en chrome des spinelles. *Bull. Mineral.*, 105(2), 197–202.

Metcalfe, A., Moune, S., Komorowski, J. C., and Moretti, R. (2022). Bottom-up vs top-down drivers of eruption style: petro-geochemical constraints from the holocene explosive activity at La Soufrière de Guadeloupe. *J. Volcanol. Geotherm. Res.*, 424, article no. 107488.

Métrich, N., Allard, P., Spilliaert, N., Andronico, D., and Burton, M. (2004). 2001 flank eruption of the alkali- and volatile-rich primitive basalt responsible of Mount Etna's evolution in the three decades. *Earth Planet. Sci. Lett.*, 228, 1–17.

Metrich, N. and Wallace, P. (2008). Volatile abundances in basaltic magmas and their degassing paths tracked by melt inclusions. *Rev. Mineral. Geochem.*, 69, 363–402.

Moretti, R. (2005). Polymerisation, basicity, oxidation state and their role in ionic modelling of silicate melts. *Ann. Geophys.*, 48(4/5), 583–608.

Moretti, R. (2021). Ionic syntax and equilibrium approach to redox exchanges in melts: basic concepts and the case of iron and sulfur in degassing magmas. In Moretti, R. and Neuville, D. R., editors, *Magma Redox Geochemistry*, volume 266 of *Geophysical Monograph, American Geophysical Union*, pages 117–138. John Wiley & Sons, Inc., Hoboken, NJ, USA.

Moretti, R., Arienzo, I., Civetta, L., Orsi, G., and D'Antonio, M. (2013a). The deep plumbing system of the Ischia island: a physico-chemical window on the fluid-saturated and CO_2-sustained Neapolitan volcanism (Southern Italy). *J. Petrol.*, 54, 951–984.

Moretti, R., Arienzo, I., Civetta, L., Orsi, G., and Papale, P. (2013b). Multiple magma degassing sources at an explosive volcano. *Earth Planet. Sci. Lett.*, 367, 95–104.

Moretti, R., Arienzo, I., Di Renzo, V., Orsi, G., Arzilli, F., Brun, F., and D'Antonio, M. (2019). Volatile segregation and generation of highly vesiculated explosive magmas by volatile-melt fining processes: the case of the Campanian Ignimbrite eruption. *Chem. Geol.*, 503, 1–14.

Moretti, R., Le Losq, C., and Neuville, D. R. (2014). The amphoteric behavior of water in silicate melts from the point of view of their ionic–polymeric constitution. *Chem. Geol.*, 367, 23–33.

Moretti, R., Métrich, N., Arienzo, I., Di Renzo, V., Aiuppa, A., and Allard, P. (2018). Degassing vs. eruptive styles at Mt. Etna volcano (Sicily, Italy). Part I: volatile stocking, gas fluxing, and the shift from low-energy to highly explosive basaltic eruptions. *Chem. Geol.*, 482, 1–17.

Moretti, R. and Neuville, D. (2021). Redox equilibria: from basic concepts to the magmatic realm. In Moretti, R. and Neuville, D. R., editors, *Magma Redox Geochemistry*, volume 266 of *Geophysical Monograph, American Geophysical Union*, pages 1–17. John Wiley & Sons, Inc., Hoboken, NJ, USA.

Moretti, R. and Ottonello, G. (2003a). A polymeric approach to the sulfide capacity of silicate slags and melts. *Metall. Mater. Trans. B*, 34, 399–410.

Moretti, R. and Ottonello, G. (2003b). Polymerization and disproportionation of iron and sulfur in silicate melts: insights from an optical basicity-based approach. *J. Non-Cryst. Solids*, 323, 111–119.

Moretti, R. and Ottonello, G. (2005). Solubility and speciation of sulfur in silicate melts: the Conjugated Toop–Samis–Flood–Grjotheim (CTSFG) model. *Geochim. Cosmochim. Acta*, 69, 801–823.

Moretti, R. and Ottonello, G. (2022). Silicate melt thermochemistry and the redox state of magmas. *Rev. Mineral. Geochem.*, 87, 339–403.

Moretti, R. and Papale, P. (2004). On the oxidation state and volatile behavior in multicomponent gas-melt equilibria. *Chem. Geol.*, 213, 265–280.

Moretti, R., Papale, P., and Ottonello, G. (2003). A model for the saturation of C–H–O–S fluids in silicate melts. In Oppenheimer, C., Pyle, D. M., and Barclay, J., editors, *Volcanic Degassing*, volume 213, pages 81–101. Geol. Soc. London Spec. Publ., London.

Moretti, R. and Stefansson, A. (2020). Volcanic and geothermal redox engines. *Elements: An Interna-*

tional Magazine of Mineralogy, Geochemistry, and Petrology, 16(3), 179–184.

Mormone, A., Piochi, M., Bellatreccia, F., De Astis, G., Moretti, R., Della Ventura, G., Cavallo, A., and Mangiacapra, A. (2011). A CO_2-rich magma source beneath the Phlegraean Volcanic District (Southern Italy): evidence from a melt inclusion study. *Chem. Geol.*, 287, 66–80.

Moussallam, Y., Edmonds, M., Scaillet, B., Peters, N., Gennaro, E., Sides, I., and Oppenheimer, C. (2016). The impact of degassing on the oxidation state of basaltic magmas: a case study of Kīlauea volcano. *Earth Planet. Sci. Lett.*, 450, 317–325.

Moussallam, Y., Longpré, M. A., McCammon, C., Gomez-Ulla, A., Rose-Koga, E. F., Scaillet, B., Peters, N., Gennaro, E., Paris, R., and Oppenheimer, C. (2019). Mantle plumes are oxidised. *Earth Planet. Sci. Lett.*, 527, article no. 115798.

Moussallam, Y., Oppenheimer, C., Scaillet, B., Gaillard, F., Kyle, P., Peters, N., Hartley, M., Berlo, K., and Donovan, A. (2014). Tracking the changing oxidation state of Erebus magmas, from mantle to surface, driven by magma ascent and degassing. *Earth Planet. Sci. Lett.*, 393, 200–209.

Nagashima, S. and Katsura, T. (1973). The solubility of sulfur in Na_2O–SiO_2 melts under various oxygen partial pressures at 1100 C, 1250 C, and 1300 C. *Bull. Chem. Soc. Jpn*, 46(10), 3099–3103.

Nash, W. M., Smythe, D. J., and Wood, B. J. (2019). Compositional and temperature effects on sulfur speciation and solubility in silicate melts. *Earth Planet. Sci. Lett.*, 507, 187–198.

Nesbitt, H. W., Bancroft, G. M., Henderson, G. S., Ho, R., Dalby, K. N., Huang, Y., and Yan, Z. (2011). Bridging, non-bridging and free (O^{2-}) oxygen in Na_2O–SiO_2 glasses: an X-ray photoelectron spectroscopic (XPS) and nuclear magnetic resonance (NMR) study. *J. Non-Cryst. Solids*, 357, 170–180.

Oppenheimer, C., Moretti, R., Kyle, P., Eschenbacher, A., Lowenstern, J., Hervig, G., and Dunbar, N. (2011). Mantle to surface gas trigger of the alkalic intraplate Erebus volcano, Antarctica. *Earth Planet. Sci. Lett.*, 306, 261–271.

Ottonello, G. (2001). Thermodynamic constraints arising from the polymeric approach to silicate slags: the system CaO–FeO–SiO_2 as an example. *J. Non-Cryst. Solids*, 282, 72–85.

Ottonello, G. (2005). Chemical interactions and configurational disorder in silicate melts. *Ann. Geophys.*, 48, 56–581.

Ottonello, G. (2021). Thermodynamic models of silicate melts. In Richet, P., Conradt, R., Takada, A., and Dyon, J., editors, *Encyclopedia of Glass Science, Technology, History, and Culture*, volume I, pages 545–558. The American Ceramic Society, John Wiley & Sons, Inc., Hoboken, New Jersey.

Ottonello, G. and Moretti, R. (2004). Lux–flood basicity of binary silicate melts. *J. Phys. Chem. Solids*, 65, 1609–1614.

Ottonello, G., Moretti, R., Marini, L., and Vetuschi Zuccolini, M. (2001). Oxidation state of iron in silicate glasses and melts: a thermochemical model. *Chem. Geol.*, 174, 157–179.

Paonita, A., Liuzzo, M., Salerno, G., Federico, C., Bonfanti, P., Caracausi, A., Giuffrida, G., La Spina, A., Caltabiano, T., Gurrieri, S., and Giudice, G. (2021). Intense overpressurization at basaltic open-conduit volcanoes as inferred by geochemical signals: the case of the Mt. Etna December 2018 eruption. *Sci. Adv.*, 7(36), article no. eabg6297.

Papale, P., Moretti, R., and Barbato, D. (2006). The compositional dependence of the saturation surface of H_2O+CO_2 fluids in silicate melts. *Chem. Geol.*, 229, 78–95.

Papale, P., Moretti, R., and Paonita, A. (2022). Thermodynamics of multi-component gas-melt equilibrium in magmas: theory, models, and applications. *Rev. Mineral. Geohem.*, 87, 431–556.

Paul, A. and Douglas, R. W. (1965). Ferric-ferrous equilibrium in binary alakali silicre glasses. *Phys. Chem. Glasses*, 6, 207–211.

Pettke, T., Halter, W. E., Webster, J. D., Aigner-Torres, M., and Heinrich, C. A. (2004). Accurate quantification of melt inclusion chemistry by LA-ICPMS: a comparison with EMP and SIMS and advantages and possible limitations of these methods. *Lithos*, 78(4), 333–361.

Pino, N. A., Moretti, R., Allard, P., and Boschi, E. (2011). Seismic precursors of a basaltic paroxysmal explosion track deep gas slug upraise. *J. Geophys. Res.*, 116, article no. B02312.

Pistone, M., Caricchi, L., and Ulmer, P. (2021). CO_2 favours the accumulation of excess fluids in felsic magmas. *Terra Nova*, 33(2), 120–128.

Roeder, P. L. and Emslie, R. (1970). Olivine-liquid equilibrium. *Contrib. Mineral. Petrol.*, 29(4), 275–289.

Rose-Koga, E. F., Bouvier, A. S., Gaetani, G. A., Wal-

lace, P. J., Allison, C. M., Andrys, J. A., Angeles de la Torre, C. A., Barth, A., Bodnar, R. J., Gartner, B., Butters, A. J. J., Castillejo, A., Chilson-Parks, B., Choudhary, B. R., Cluzel, N., Cole, M., Cottrell, E., Daly, A., Danyushevsky, L. V., DeVitre, C. L., Drignon, L. J., France, L., Gaborieau, M., Garcia, M. O., Gatti, E., Genske, F. S., Hartley, M. E., Hughes, E. C., Iveson, A. A., Johnson, E. R., Jones, M., Kagoshima, T., Katzir, Y., Kawaguchi, M., Kawamoto, T., Kelley, K. A., Koornneef, J. M., Kurz, M. D., Laubier, M., Layne, G. D., Lerner, A., Lin, K.-Y., Liu, P.-P., Lorenzo-Merino, A., Luciani, N., Magalhães, N., Marschall, H. R., Michael, P. J., Monteleone, B. D., Moore, L. R., Moussallam, Y., Muth, M., Myers, M. L., Narváez, D. F., Navon, O., Newcombe, M., Nichols, A. R. L., Nielsen, R. L., Pamukcu, A., Plank, T., Rasmussen, D. J., Roberge, J., Schiavi, F., Schwartz, D. M., Shimizu, K., Shimizu, K., Shimizu, N., Thomas, J. B., Thompson, G. T., Tucker, J. M., Ustunisik, G., Waelkens, A., Zhang, Y., and Zhou, T. (2021). Silicate melt inclusions in the new millennium: a review of recommended practices for preparation, analysis, and data presentation. *Chem. Geol.*, 570, article no. 120145.

Sakai, H., Casadevall, T. J., and Moore, J. G. (1982). Chemistry and isotope ratios of sulfur in basalts and volcanic gases at Kilauea Volcano, Hawaii. *Geochim. Cosmochim. Acta*, 46, 729–738.

Sato, M. and Moore, J. G. (1973). Oxygen and sulfur fugacities of magmatic gases directly measured in active vents of Mount Etna. *Phil. Trans. R. Soc. Lond. Ser. A*, 274, 137–146.

Schiano, P. (2003). Primitive mantle magmas recorded as silicate melt inclusions in igneous minerals. *Earth-Sci. Rev.*, 63, 121–144.

Shinohara, H. (2008). Excess degassing from volcanoes and its role on eruptive and intrusive activity. *Rev. Geophys.*, 46, article no. RG4005. 1–31.

Spilliaert, N., Allard, P., Métrich, N., and Sobolev, A. V. (2006). Melt inclusion record of the conditions of ascent, degassing, and extrusion of volatile-rich alkali basalt during the powerful 2002 flank eruption of Mount Etna (Italy). *J. Geophys. Res.*, 111, article no. B04203. 1–19.

Temkin, M. (1945). Mixtures of fused salts as ionic solutions. *Acta Phys. Chem. USSR*, 20, 411–420.

Tomasi, J., Mennucci, B., and Cancès, E. (1999). The IEF version of the PCM solvation method: an overview of a new method addressed to study molecular solutes at the QM ab initio level. *J. Mol. Struct.*, 464, 211–226.

Tomasi, J. and Persico, M. (1994). Molecular interactions in solution: an overview of methods based on continuous distributions of the solvent. *Chem. Rev.*, 94, 2027–2094.

Toop, G. W. and Samis, C. S. (1962a). Activities of ions in silicate melts. *Trans. Met. Soc. AIME*, 224, 878–887.

Toop, G. W. and Samis, C. S. (1962b). Some new ionic concepts of silicate slags. *Can. Metall. Q.*, 1, 129–152.

Tramontano, S., Gualda, G. A., and Ghiorso, M. S. (2017). Internal triggering of volcanic eruptions: tracking overpressure regimes for giant magma bodies. *Earth Planet. Sci. Lett.*, 472, 142–151.

Trémillon, B. (1974). *Chemistry in Non-Aqueous Solvents*. D. Reidel Publishing Company, Dordrecht. page 285.

Utami, S. B., Costa, F., Lesage, P., Allard, P., and Humaida, H. (2021). Fluid fluxing and accumulation drive decadal and short-lived explosive basaltic andesite eruptions preceded by limited volcanic unrest. *J. Petrol.*, 62(11), article no. egab086.

Venugopal, S., Schiavi, F., Moune, S., Bolfan-Casanova, N., Druitt, T., and Williams-Jones, G. (2020). Melt inclusion vapour bubbles: the hidden reservoir for major and volatile elements. *Sci. Rep.*, 10(1), 1–14.

Vigouroux, N., Wallace, P. J., and Kent, A. J. (2008). Volatiles in high-K magmas from the western trans-Mexican volcanic belt: evidence for fluid fluxing and extreme enrichment of the mantle wedge by subduction processes. *J. Petrol.*, 49(9), 1589–1618.

Wallace, P. and Carmichael, I. S. E. (1992). Sulfur in basaltic magmas. *Geochim. Cosmochim. Acta*, 56, 1863–1874.

Wallace, P. and Carmichael, I. S. E. (1994). S speciation in submarine basaltic glasses as determined by measurements of Ska X-ray wavelength shifts. *Am. Mineral.*, 79, 161–167.

Wallace, P. J. and Edmonds, M. (2011). The sulfur budget in magmas: evidence from melt inclusions, submarine glasses, and volcanic gas emissions. *Rev. Mineral. Geochem.*, 73(1), 215–246.

Wallace, P. J., Kamenetsky, V. S., and Cervantes, P. (2015a). Melt inclusion CO_2 contents, pressures of olivine crystallization, and the problem of shrinkage bubbles. *Am. Mineral.*, 100(4), 787–794.

Wallace, P. J., Plank, T., Edmonds, M., and Hauri, E. H. (2015b). Volatiles in magmas. In *The Encyclopedia of Volcanoes*, pages 163–183. Academic Press, San Diego, San Francisco, New York, Boston, London, Sidney, Toronto.